Computer Methods in Applied Mechanics and Engineering 419 (2024) 116685

Contents lists available at ScienceDirect

Comput. Methods Appl. Mech. Engrg.

journal homepage: www.elsevier.com/locate/cma

Development of process design tools for extrusion-based bioprinting: From numerical simulations to nomograms through reduced-order modeling

Francesco Chirianni *, Giuseppe Vairo, Michele Marino

University of Rome Tor Vergata, Department of Civil Engineering and Computer Science Engineering, via del Politecnico 1, Rome, 00133, Italy

ARTICLE INFO

Keywords:
Computational methods for bioprinting
Reduced-order modeling
Non-Newtonian fluid dynamics
Bioprinting
Process design tools

ABSTRACT

The planning of a bioprinting procedure requires the definition of several process variables. In extrusion-based bioprinting these are, for instance, the printing pressure, the nozzle diameter, the target extrusion velocity and/or mass flow rate. They should be properly set in order to allow printability of the bio-ink, as well as to ensure high cell viability at the end of the process. In fact, printing procedures expose cells to shear and extensional stresses that can lead to mechanobiological damage mechanisms. Bioprinting planning is then a challenging task since process variables are closely interconnected each other through the physical response of bio-inks. Non-Newtonian characteristics of bio-inks, together with possible complex geometries of the extruding system, generally introduce a strong non-linear coupling among process variables. To date, the bioprinting planning in laboratory practice is generally performed via expensive and time-consuming trial-and-error procedures. The aim of this work is the development of novel methodological approaches for an informed definition of printing process variables such to guarantee target conditions of the outcome. The non-linear coupling among dominant process variables is described via a semi-analytical approach, calibrated through high-fidelity numerical solutions and defined via a reduced-order modeling strategy. A cell damage law depending on bioprinting conditions is also introduced, generalizing state-of-the-art approaches on the basis of available experimental evidence. The proposed framework allows to build operative nomograms, whose practical utility is confirmed via some exemplary applications. The latter address the prediction of extrusion velocity, mass flow rate and cell viability, when both the printing pressure and nozzle diameter vary within typically-adopted ranges. The analyzed case studies highlight soundness and effectiveness of such a modeling strategy in providing a clear and straight pathway for planning and setup of bioprinting processes.

1. Introduction

Bioprinting is an additive manufacturing technology used to fabricate artificial cell-laden constructs for various tissue engineering applications [1–8]. In particular, with reference to the extrusion-based technique [9–11], a suspension of viable cells and biomaterials, often referred to as bio-ink [12], is loaded into the printing system, extruded through a syringe with varying cross-section and deposited layer-by-layer on a platform to build a three-dimensional construct [13].

Notwithstanding recent advancements in this research field, there are still many open issues and challenging tasks pertaining to the planning of a bioprinting procedure [14–19] and the optimal setting of the involved process variables [20–22]. By referring to

* Corresponding author.
E-mail addresses: chirianni@ing.uniroma2.it (F. Chirianni), vairo@ing.uniroma2.it (G. Vairo), m.marino@ing.uniroma2.it (M. Marino).

https://doi.org/10.1016/j.cma.2023.116685
Received 18 September 2023; Received in revised form 14 November 2023; Accepted 4 December 2023

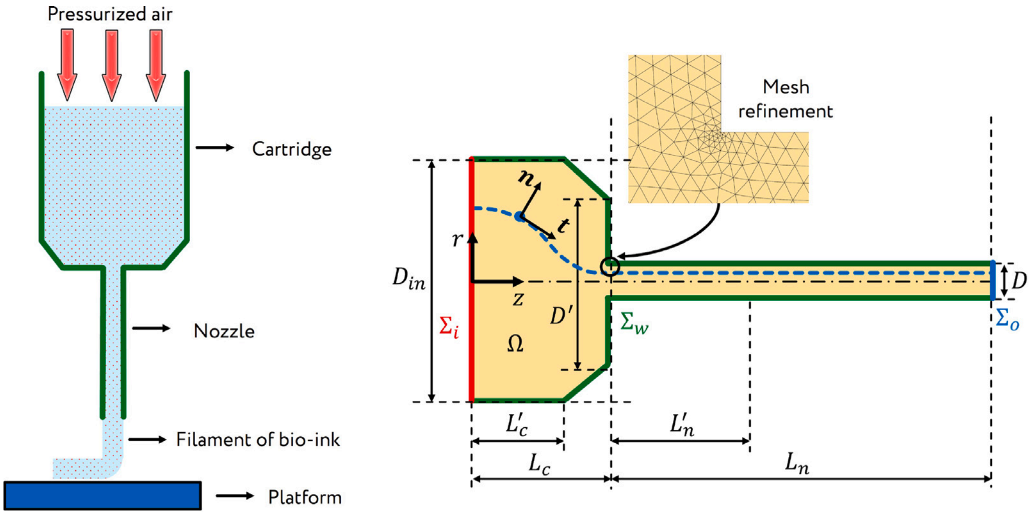

Fig. 1. Schematic representation of the extrusion process (on the left). Extrusion domain (analogous to the one reported in [27]); notation and a detail of the computational mesh adopted in high-fidelity CFD simulations (on the right).

extrusion-based bioprinting, typical process variables are the printing pressure, the nozzle diameter, the target extrusion velocity and/or the mass flow rate. Their optimal choice is strictly dependent on the specific application, and they should be set not only to fulfill technological demands (e.g., printability, process speed, resolution) but also in order to ensure the highest cell viability at the end of the process [15]. As a matter of fact, the printing mechanisms expose cells to mechanical stresses that can induce damage phenomena, generally associated to the disruption of the outer cell membrane or the onset of apoptotic signals [23–26]. In particular, possible cell damage is produced by dominant shear effects affecting the bio-ink flowing through the extruder nozzle [27–29], and/or by extensional mechanisms to which cells dispersed into the bio-ink undergo as a result of the abrupt cross-section reduction that usually characterizes the extruder geometry at the nozzle inlet [13,27,30,31].

The optimal setting of process variables is further complicated by non-linear and coupled relationships among process variables [20,32], often affected by counteracting needs. For instance, high mass flow rate is desirable to speed-up printing operations but, at the same time, it generally leads to high stresses that may affect cell viability [33]. Nozzles with small diameter allow to obtain high printing resolutions but these are associated also with high printing pressures, potentially leading to low printability and increased risk of cell damage [15,27–29,34,35]. To date, bioprinting planning in the laboratory practice is generally based on heuristic approaches, leading to expensive and time-consuming trial-and-error attempts [32].

In this context, the present work proposes a novel methodological strategy towards a rational and effective planning of bioprinting procedures. The bio-ink fluid-dynamics associated to the extrusion process is numerically reproduced by modeling the bio-ink as an incompressible non-Newtonian viscous fluid, characterized by a shear-thinning rheological behavior. Furthermore, a measure of cell viability is established on the basis of a novel cell damage model. The latter is formulated in agreement with the experimental evidence available in literature, by generalizing the shear-based approach proposed by Han et al. [28] with a description of cell distributions within the nozzle during extrusion, and accounting for extensional mechanisms. High-fidelity numerical simulations are employed to define and calibrate a semi-analytical reduced-order modeling approach that introduces straightforward relationships among coupled fundamental process variables. Based on these relationships, process-specific nomograms are built, furnishing useful and simple design tools for planning extrusion-based bioprinting processes via fast graphical indications. Such nomograms allow, for instance, to easily obtain how the extrusion velocity, mass flow rate and cell viability are affected by both nozzle diameter and printing pressure, or otherwise how the printing pressure should be varied to guarantee a constant extrusion velocity, mass flow rate or cell viability when different nozzle diameters are employed. The proposed computational workflow is calibrated and validated using existing experimental evidence on two case studies with different bio-inks composition [28].

2. Materials and methods

In the present section, theoretical and computational modeling strategies adopted to describe the bio-ink extrusion process and cell damage mechanisms are introduced.

2.1. Bio-ink extrusion description

The extrusion bioprinting process is modeled by describing the bio-ink as an incompressible and non-Newtonian viscous fluid, undergoing a laminar and isothermal flow regime when an inlet–outlet pressure difference is applied [27,36,37]. By referring to the notation defined in Fig. 1, the cylindrical coordinate system (r, θ, z) is introduced with unit basis vectors $\boldsymbol{e}_r$, $\boldsymbol{e}_\theta$ and $\boldsymbol{e}_z$. The extrusion domain Ω is considered as axisymmetric, the symmetry axis being coincident with the z-axis. Moreover, the boundary $\partial\Omega$ is regarded as $\partial\Omega = \Sigma_w \cup \Sigma_i \cup \Sigma_o$, where Σ_w, Σ_i and Σ_o identify, respectively, the rigid wall of the extrusion domain Ω (comprising cartridge and nozzle contiguous regions), the inflow cross-section of the cartridge at $z = 0$, and the outflow cross-section of the nozzle at $z = L_c + L_n$. Here, L_c and L_n are the cartridge and nozzle lengths, respectively. By disregarding any effect induced by volume forces, the steady-state response of the bio-ink is described by the following differential problem:

Problem 1. Find the velocity field $\boldsymbol{v}(r,\theta,z) = v_r\boldsymbol{e}_r + v_\theta\boldsymbol{e}_\theta + v_z\boldsymbol{e}_z$ and the pressure field $p(r,\theta,z)$ such that:

$$\nabla\cdot\boldsymbol{v} = 0 \quad \text{in } \Omega \tag{1a}$$

$$\rho\,\boldsymbol{v}\cdot\nabla\boldsymbol{v} = -\nabla p + \nabla\cdot\boldsymbol{\tau} \quad \text{in } \Omega \tag{1b}$$

$$\boldsymbol{v} = \boldsymbol{0} \quad \text{on } \Sigma_w \tag{1c}$$

$$\boldsymbol{v} = \hat{v}_z(r)\boldsymbol{e}_z \quad \text{on } \Sigma_i \tag{1d}$$

$$\left[(-p\boldsymbol{I} + \boldsymbol{\tau})\boldsymbol{e}_z\right]\cdot\boldsymbol{e}_z = -\hat{p} \quad \text{on } \Sigma_o \tag{1e}$$

where ρ is the bio-ink density (assumed to be constant), $\boldsymbol{\tau}$ is the symmetric second-order deviatoric stress tensor, $\hat{v}_z$ and $\hat{p}$ are assigned inlet velocity and outlet pressure profiles, respectively.

The symmetric second-order deviatoric stress tensor $\boldsymbol{\tau}$ is described by a generalized Newtonian law, reading [38]:

$$\boldsymbol{\tau} = 2\mu(\dot{\gamma})\boldsymbol{D} = \mu(\dot{\gamma})\left[\nabla\boldsymbol{v} + (\nabla\boldsymbol{v})^T\right], \tag{2}$$

where the second-order strain-rate tensor $\boldsymbol{D}$ corresponds to the symmetric part of the velocity gradient $\nabla\boldsymbol{v}$, and μ is the dynamic viscosity. The latter is assumed to depend on $\boldsymbol{D}$ via the shear rate $\dot{\gamma} = \sqrt{2J_2(\boldsymbol{D})}$, with $J_2 = \boldsymbol{D}:\boldsymbol{D}$ being the second main strain-rate invariant.

The rheological behavior of the bio-ink is described by the 5-parameter Carreau–Yasuda model [39]:

$$\mu(\dot{\gamma}) = \mu_\infty + \left(\mu_0 - \mu_\infty\right)\left[1 + (\lambda\dot{\gamma})^a\right]^{\frac{n-1}{a}}, \tag{3}$$

where μ_0 is the dynamic viscosity as $\dot{\gamma} = 0$, μ_∞ is the asymptotic value of μ when $\dot{\gamma} \to \infty$, λ is a relaxation time constant, a is a dimensionless parameter, and n is a power-law exponent [24]. Bio-inks generally exhibit a shear-thinning behavior [12,40–42], that is the dynamic viscosity decreases as the shear rate increases, obtained from Eq. (3) when $\mu_0 > \mu_\infty$ and $0 \le n < 1$.

Given the problem symmetry, both pressure and velocity unknown fields do not depend on the angular coordinate θ and $v_\theta = 0$ everywhere in Ω. Hence, the deviatoric stress tensor $\boldsymbol{\tau}$, the strain rate tensor $\boldsymbol{D}$ and the shear rate $\dot{\gamma}$ read:

$$\boldsymbol{\tau} = \begin{bmatrix} \tau_{rr} & 0 & \tau_{rz} \\ 0 & \tau_{\theta\theta} & 0 \\ \tau_{rz} & 0 & \tau_{zz} \end{bmatrix}, \tag{4}$$

$$\boldsymbol{D} = \begin{bmatrix} D_{rr} & 0 & D_{rz} \\ 0 & D_{\theta\theta} & 0 \\ D_{rz} & 0 & D_{zz} \end{bmatrix} = \begin{bmatrix} \frac{\partial v_r}{\partial r} & 0 & \frac{1}{2}\left(\frac{\partial v_r}{\partial z} + \frac{\partial v_z}{\partial r}\right) \\ 0 & \frac{v_r}{r} & 0 \\ \frac{1}{2}\left(\frac{\partial v_r}{\partial z} + \frac{\partial v_z}{\partial r}\right) & 0 & \frac{\partial v_z}{\partial z} \end{bmatrix}, \tag{5}$$

$$\dot{\gamma} = \left\{\left(\frac{\partial v_z}{\partial r} + \frac{\partial v_r}{\partial z}\right)^2 + 2\left[\left(\frac{\partial v_r}{\partial r}\right)^2 + \left(\frac{v_r}{r}\right)^2 + \left(\frac{\partial v_z}{\partial z}\right)^2\right]\right\}^{1/2}. \tag{6}$$

Therefore, given the incompressibility condition in Eq. (1a), the power of internal forces per unit volume w results in [43]:

$$w = (-p\boldsymbol{I} + \boldsymbol{\tau}) : \boldsymbol{D} = \left(\tau_{zz} - \tau_{rr}\right)D_{zz} + \left(\tau_{\theta\theta} - \tau_{rr}\right)D_{\theta\theta} + 2\tau_{rz}D_{rz}. \tag{7}$$

In order to describe cell damage mechanisms, it is convenient to decouple extensional and shear effects within the power density w. To this aim, let a local reference system $(\mathbf{n},\mathbf{t})$ be introduced, where $\mathbf{t}(r,z)$ and $\mathbf{n}(r,z)$ denote respectively the tangent and normal unit vectors to a bio-ink particle trajectory (see Fig. 1). Accordingly, the power of internal forces per unit volume can be written as:

$$w = \left(\tau_{tt} - \tau_{nn}\right)D_{tt} + \left(\tau_{\theta\theta} - \tau_{nn}\right)D_{\theta\theta} + 2\tau_{nt}D_{nt} = w_e + w_s, \tag{8}$$

where w_e and w_s identify the rates of viscous dissipation induced respectively by extensional and shear effects, reading:

$$w_e = \left(\tau_{tt} - \tau_{nn}\right)D_{tt} + \left(\tau_{\theta\theta} - \tau_{nn}\right)D_{\theta\theta}, \tag{9a}$$

$$w_s = 2\tau_{nt}D_{nt}. \tag{9b}$$

The extensional dissipation w_e can be also expressed as $w_e = \tau_e\dot{\epsilon}$, where τ_e is the extensional stress and $\dot{\epsilon}$ is the extensional stretch rate. The latter is defined from the third principal strain-rate invariant $I_3(\boldsymbol{D}) = \det\boldsymbol{D}$ as [44,45]:

$$\dot{\epsilon} = \frac{6\,I_3(\boldsymbol{D})}{J_2(\boldsymbol{D})} = \frac{6\det\boldsymbol{D}}{\boldsymbol{D}:\boldsymbol{D}}. \tag{10}$$

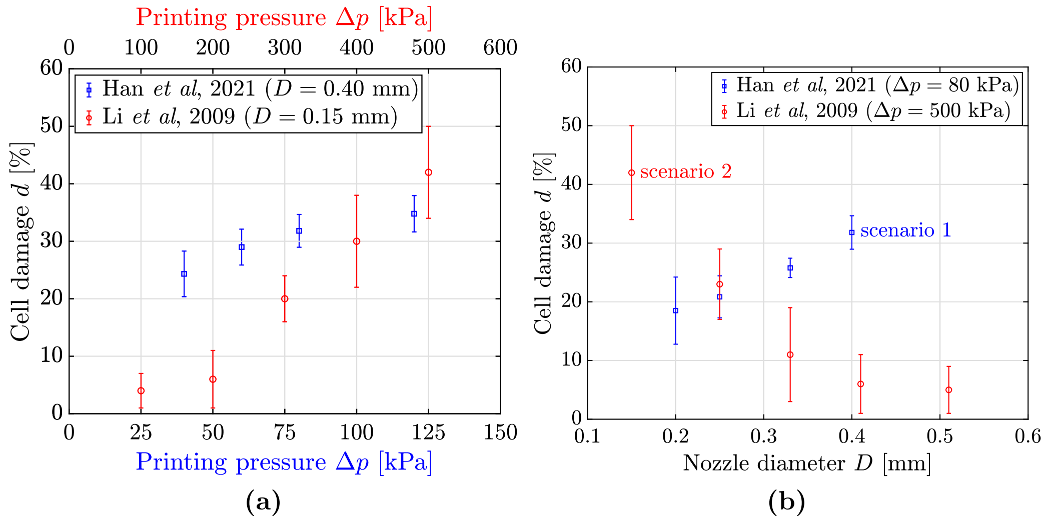

Fig. 2. Cell damage experimental measurements from Han et al. [28] (human dermal fibroblasts suspended in a 3 wt% alginate-based aqueous solution) and Li et al. [29] (murine 3T3 fibroblasts suspended in a 6 wt% alginate-based aqueous solution). (a) Evolution of cell damage when Δp varies at fixed D. (b) Evolution of cell damage when D varies at fixed Δp.

Hence, by combining Eqs. (9a) and (10), the extensional stress τ_e reads:

$$\tau_e = \frac{w_e}{\dot{\varepsilon}} = \frac{\left[\left(\tau_{tt} - \tau_{nn}\right) D_{tt} + \left(\tau_{\theta\theta} - \tau_{nn}\right) D_{\theta\theta}\right] J_2(\boldsymbol{D})}{6\, I_3(\boldsymbol{D})}\,. \tag{11}$$

2.2. Cell damage modeling

During extrusion cells may experience damage. Due to the low cell volume fractions in typical bio-inks, cell–cell interactions are not believed to play a major role on cell damage, which is instead attributed only to mechanical stresses induced by the interaction between cells and the surrounding material [28]. Furthermore, it can be generally assumed that stresses acting on cells are well-approximated by local stresses associated to the flow conditions of the equivalent homogeneous fluid describing the bio-ink [13,46]. Bio-ink flow is strongly affected by the extruder geometries, typically characterized by an abrupt contractive region connecting the cartridge body to the nozzle (see Fig. 1). Accordingly, when the bio-ink flows through such a contractive region, fluid particles undergo significant extensional effects; on the other hand, when the bio-ink is forced to flow through the nozzle, shear effects become dominant [27]. Specifically, shear effects are commonly considered the main cause of cell damage [28,40,47–49], with shear-based damage mechanisms mainly influenced by both shear stress level and stress exposure time [27,29,50] or travel distance in the nozzle [28].

Let the scalar d be introduced as a global measure of cell damage at the end of the extrusion process, so that $d = 0$ (respectively, $d = 1$) means that all cells are alive (respectively, dead). Accordingly, cell viability c_v at the end of the extrusion process is quantified as:

$$c_v = 1 - d\,. \tag{12}$$

Experimental evidence obtained with cylindrical nozzles highlights that, for a given nozzle diameter D, the cell damage d increases with the printing pressure Δp [15,27–29,34,35] (see Fig. 2(a)). On the other hand, when the printing pressure Δp is fixed and the nozzle diameter D increases, experimental results reported in literature indicate that cell damage d may either increase [27,28] (scenario 1 in Fig. 2(b)) or decrease [29,34,35] (scenario 2 in Fig. 2(b)). The multifactorial nature of cell damage does not allow to exclude that both scenarios are trustable, possibly depending on the cell type, biophysical properties of the hydrogel comprising the bio-ink, and flow conditions. Thereby, a damage model able to reproduce both the previously-introduced behaviors is here developed.

2.2.1. State-of-the-art approach: the damage model by Han et al. (2021)

In the state-of-the-art, Han et al. in [28] proposed a cell damage law derived from the logistic differential equation and validated towards a wide range of bioprinting conditions. The damage law proposed in [28] reads:

$$d \equiv d^H(W_p) = d_{max} - \left(d_{max} - d_0\right) \exp\left(-a_p W_p\right), \tag{13}$$

where W_p is the pressure work, that is a measure of the energy required to move fluid particles against pressure forces, and $a_p > 0$, $d_0 \geq 0$ and $d_{max} > 0$ are model parameters, with a_p governing the sensitivity of cell damage by W_p, d_0 being a reference measure of

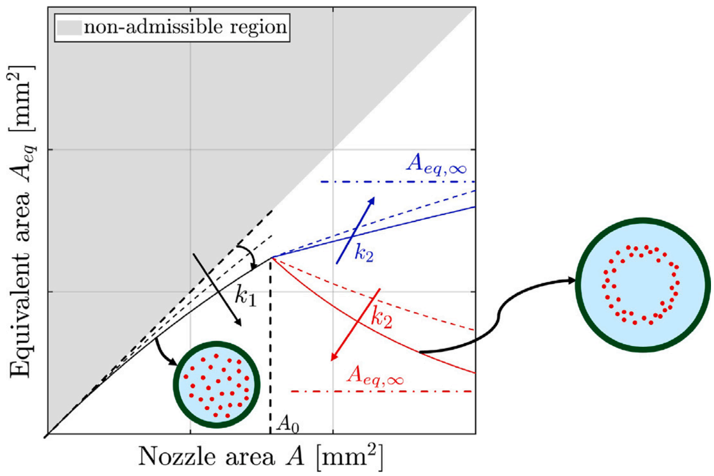

Fig. 3. Equivalent area A_{eq} (interested by cell distribution) vs. nozzle area A. Qualitative description of the influence of model parameters introduced in Eq. (16).

the cell damage at the inlet section of the nozzle and d_{max} being the asymptotic damage level for high values of W_p. The damage law in Eq. (13) is specialized to the case of a cylindrical nozzle of diameter D and length L_n by observing that the pressure field in the nozzle is linearly depending on the axial coordinate z, that is $p(z) = (\Delta p_n/L_n)(L_c + L_n - z)$ (see Fig. 1), where Δp_n denotes the total pressure drop in the nozzle. Accordingly, in this case the pressure work W_p reads [28]:

$$W_p = A \int_{L_c}^{L_c+L_n} p(z)\, dz = \frac{1}{2} \Delta p_n A L_n\,, \tag{14}$$

where $A = \pi D^2/4$ is the nozzle cross-section area. For cylindrical nozzles, W_p in Eq. (14) can be equivalently formulated as $W_p = (3\overline{\tau_s} L_n/D) A L_n$, where $\overline{\tau_s} = \Delta p_n D/(6L_n)$ is the average shear stress over the nozzle cross-section, hence combining the effects of both shear stresses and travel distance. Given the proportionality between W_p and $\overline{\tau_s}$, the damage law by Han et al. (2021) in Eq. (13) describes then only shear-related damage.

Finally, it is noteworthy that, when a fixed value of Δp_n is considered, the pressure work W_p in Eq. (14) is directly proportional to the nozzle diameter D, Eq. (13) describing only damage in agreement with experimental evidence in scenario 1, but not in scenario 2 (see Fig. 2(b)).

2.2.2. Proposed generalized model

In order to introduce a damage law able to overcome limitations of the previously-recalled cell damage model, two generalizations related to the definition of the pressure work W_p and to the model parameter d_0 are proposed in the following.

- **The equivalent pressure work**. Aiming to introduce a damage law able to account also for the possible cell damage reduction when, for a fixed printing pressure, the nozzle diameter increases, a generalization in the definition of the pressure work is proposed. In particular, an equivalent pressure work W_p^{eq} is introduced as:

$$W_p^{eq} = \frac{1}{2} \Delta p_n A_{eq} L_n\,, \tag{15}$$

defined in terms of an equivalent nozzle area $A_{eq} \le A$. This choice is justified since cells are not necessarily evenly distributed over the entire nozzle cross-section. In fact, referring to solid particles dispersed within a fluid flow in a channel, several studies show that the distribution of particles over the channel cross-section may vary, for instance, with the rheological properties of the fluid and the ratio of channel to particle diameter [51–53]. Hence, A_{eq} identifies a measure of the area portion of the nozzle cross-section interested by cell distribution and it is here described as:

$$A_{eq}(A) := \begin{cases} A \exp\left(-k_1 A\right) & \text{if } 0 < A \le A_0 \\ A_{eq,0} + (A_{eq,\infty} - A_{eq,0})\left[1 - \exp\left(-k_2\left(A - A_0\right)\right)\right] & \text{if } A > A_0 \end{cases}\,, \tag{16}$$

with $A_0 > 0$, $A_{eq,\infty} > 0$, $k_1 \ge 0$ and $k_2 \ge 0$ being model parameters and $A_{eq,0} = A_0 \exp\left(-k_1 A_0\right)$. As shown in Fig. 3, very different relationships between the effective A_{eq} and the total A nozzle areas are permitted by Eq. (16), such to reproduce a variety of experimental outcomes. In particular, as it will be shown in the following (see Section 3), the proposed generalization of the pressure work allows to describe both experimental scenarios depicted in Fig. 2(b).

- **Extensional-induced damage effects**. The damage model proposed in [28] is herein further generalized in order to describe the experimental evidence that some cell lines are particularly sensitive to extensional stresses [27,54,55]. As previously outlined, and as numerical results presented in the following prove (see Section 3), extensional stresses are significant at the contractive region of the cartridge–nozzle connection, and specifically close to the inlet nozzle cross-section, while shear stresses are dominant in the nozzle.
  Accordingly, Eq. (13) is regarded as describing damage occurring within the nozzle domain only. Extensional damage is accounted for by characterizing the damage level at the nozzle entrance as function of extensional stresses, namely by providing a non-constant description of the quantity d_0. Cells are exposed to extensional stresses only within the contractive range, and then for a very short time period/travel distance when compared to shear-stress effects in the nozzle. Thus, the extensional cell damage is assumed to be related only to the magnitude of the extensional stresses [27], and in particular to their average measure $\overline{\tau_e}$ at the nozzle inlet (i.e., at $z = L_c$, Fig. 1), that can be computed via Eq. (11) as:
  $$\overline{\tau_e} = \frac{1}{A} \int_0^{D/2} \tau_e\big|_{z=L_c} \, 2\pi r \, dr \,. \tag{17}$$
  Following the approach proposed in [27], the cell damage d_e induced by extensional mechanisms is described as:
  $$d_e(\overline{\tau_e}) = d_{e,max} \left[1 - \exp\left(-a_e \overline{\tau_e}^{\,b_e} \right) \right] , \tag{18}$$
  where $d_{e,max} \geq 0$, $a_e > 0$ and $b_e > 0$ are model parameters.

Therefore, by considering $d_0 = d_e(\overline{\tau_e})$ and by replacing W_p with W_p^{eq} in Eq. (13), the cell damage law proposed in this work reads:

$$d(W_p^{eq}, \overline{\tau_e}) = d_{max} - \left\{ d_{max} - d_{e,max} \left[1 - \exp\left(-a_e \overline{\tau_e}^{\,b_e} \right) \right] \right\} \exp\left(-a_p W_p^{eq} \right) . \tag{19}$$

For a comparison between damage mechanisms, the extensional damage law d_e in Eq. (18) will be compared with a measure of cell damage d_s caused by shear stress only, estimated as:

$$d_s(W_p^{eq}, \overline{\tau_e}) = d(W_p^{eq}, \overline{\tau_e}) - d_e(\overline{\tau_e}) \,. \tag{20}$$

2.3. High-fidelity models: CFD simulations

The analytical solution of a Carreau–Yasuda fluid flow problem described by Eqs. (1a)–(1e) within general extruder geometries is generally not possible [24]. Thus, computational fluid dynamics (CFD) simulations have been performed by using a mixed Galerkin finite-element formulation. The computational domain describing the axisymmetric geometry in Fig. 1 is discretized via axisymmetric P_2P_1 triangular elements in the (r, z) plane. The finite-element formulation is implemented through the AceGen package of Wolfram Mathematica [56,57]. Velocity and pressure fields are interpolated via quadratic and linear lagrangian shape functions, respectively. Such a finite-element formulation belongs to the Taylor–Hood family of Stokes elements that satisfies the inf–sup stability condition [58].

In bioprinting applications the expected Reynolds numbers are in the range $10^{-5} \div 10^{-1}$, since the bio-ink density, the extrusion velocity, the nozzle diameter and the bio-ink dynamic viscosity are in the order of 10^3 kg/m^3, 10^{-2} m/s, 10^{-4} m and $10^{-2} \div 10^2$ Pa s, respectively. Hence, a laminar flow regime can be considered. Moreover, since a fully-developed state is expected to be attained within the nozzle close to the contractive region, a reduced length $L_n' < L_n$ can be considered for the nozzle domain in order to reduce the computational effort. Based upon mesh sensitivity analyses, 45 000 ÷ 55 000 elements are considered in the geometric discretization of the domain. Meshes are refined at the cartridge–nozzle connection, where the highest gradients in the solution are expected. Consistently with the differential problem introduced in Section 2.1, the following boundary conditions have been implemented (see notations in Fig. 1):

- the velocity profile at the inlet section (i.e., at $z = 0$) is defined by referring to the velocity profile of a Newtonian–Poiseuille flow, that is by prescribing $\hat{v}_z = 2\left[\overline{v}(D/D_{in})^2\right]\left[1 - (2r/D_{in})^2\right]$, where $\overline{v}$ is the mean outflow velocity;
- the pressure profile at the computational outflow boundary (i.e., at $z = L_c + L_n'$) is prescribed as uniform and equal to zero, as a reference value.

The choice to impose a Newtonian velocity profile at the inlet boundary is justified by the fact that the low mean inflow velocity and the large inlet diameter are associated with low shear rates; therefore, close to the inlet region the fluid behaves like a Newtonian one with dynamic viscosity equal to μ_0.

In order to perform post-processing analyses, numerical CFD solutions have been employed to compute the following quantities:

- the pressure drop Δp_c in the contractive region of the extruder, that is for $0 \leq z \leq L_c$;
- the average extensional stress $\overline{\tau_e}$ as defined in Eq. (17);
- the pressure drop per unit length $\Delta p_n / L_n$ in the nozzle, that is for $L_c \leq z \leq L_c + L_n$, and estimated from CFD results as:
  $$\frac{\Delta p_n}{L_n} \simeq \frac{p|_{z=L_c} - p|_{z=L_c+L_n'}}{L_n'} \,. \tag{21}$$

2.4. Reduced-order model and nomograms

The results obtained from CFD simulations have been used to build a reduced-order (semi-analytical) model able to synthetically describe the relationships among fundamental process variables. In detail, the post-processing quantities Δp_c, $\overline{\tau_e}$ and Δp_n are normalized with respect to the following process variables:

- fluid properties: bio-ink density ρ and average measure $\overline{\mu}$ of the dynamic viscosity, defined as $\overline{\mu} = (\mu_0 + \mu_\infty)/2$;
- extrusion settings: mean outflow velocity $\overline{v}$;
- geometric features: nozzle diameter D and diameter D_{in} of the inlet section for Δp_c and $\overline{\tau_e}$; nozzle diameter D and nozzle length L_n for Δp_n.

By applying the Buckingham π Theorem for dimensional analysis [59], the following relationships can be obtained for the normalized post-processing quantities (indicated via the superscript n):

$$\Delta p_c^n = \frac{\Delta p_c}{\frac{\overline{\mu}\,\overline{v}}{D}} = f\left(Re, \frac{D}{D_{in}}\right), \tag{22a}$$

$$\overline{\tau_e}^n = \frac{\overline{\tau_e}}{\frac{\overline{\mu}\,\overline{v}}{D}} = g\left(Re, \frac{D}{D_{in}}\right), \tag{22b}$$

$$\left(\frac{\Delta p_n}{L_n}\right)^n = \frac{\Delta p_n}{L_n}\frac{D^2}{\overline{\mu}\,\overline{v}} = h\left(Re, \frac{D}{L_n}\right), \tag{22c}$$

where $Re = (\rho\overline{v}D)/\overline{\mu}$ is a reference Reynolds number, and f, g and h are dimensionless functions to be determined. Inspired by a generalized form of the Hagen–Poiseuille law, Eqs. (22a)–(22c) are expressed via power-law relationships:

$$y = \alpha_y(\xi) Re^{-\beta_y(\xi)}, \tag{23}$$

where $y = \Delta p_c^n$ and $\xi = D/D_{in}$ for Eq. (22a), $y = \overline{\tau_e}^n$ and $\xi = D/D_{in}$ for Eq. (22b) and $y = (\Delta p_n/L_n)^n$ and $\xi = D/L_n$ for Eq. (22c). Moreover, quantities α_y and β_y are expressed, in turn, as power-law functions of the corresponding dimensionless geometric ratio ξ:

$$\alpha_y(\xi) = \alpha_{y,1}\xi^{\alpha_{y,2}} + \alpha_{y,3}, \tag{24a}$$

$$\beta_y(\xi) = \beta_{y,1}\xi^{\beta_{y,2}} + \beta_{y,3}, \tag{24b}$$

parameters $\alpha_{y,i}$ and $\beta_{y,i}$ (with $i = 1, 2, 3$) being determined via a 2-step calibration procedure described in Appendix A. It is noteworthy that, since the non-Newtonian character of the bio-ink, coefficients $\alpha_{y,i}$ and $\beta_{y,i}$ are expected to be dependent on the rheological properties of the fluid.

Once such a reduced-order model has been calibrated, specific bio-ink nomograms can be built. Such diagrams graphically summarize the non-linear relationships among five important coupled process variables:

- two process inputs: the nozzle diameter D and the printing pressure Δp;
- three process outputs: the mass flow rate $\dot{m}$, the extrusion velocity $\overline{v}$, and the cell viability c_v.

Nomograms are here built in the plane of printing pressures Δp and nozzle diameters D. Three families of isopleths are obtained: at constant mass flow rate $\dot{m}$, at constant extrusion velocity $\overline{v}$ and at constant cell viability c_v. In detail, the printing pressure Δp is evaluated as $\Delta p = \Delta p_c + \Delta p_n$, where Δp_c and Δp_n are determined from Eqs. (22a) and (22c); the extrusion velocity $\overline{v}$ results from the continuity condition $\dot{m} = \rho A\overline{v}$ when isopleths for constant values of $\dot{m}$ are addressed; the non-linear system defined by Eqs. (12), (15), (19), (22b) and (22c) is solved in the case of isopleths for constant values of c_v.

3. Results and discussion

Alginate-based hydrogels mixed with human dermal fibroblasts CCD-986sk (CRL-1947, ATCC, Rockville, MD, USA) are considered as bio-inks. Cell density is equal to $1.5 \div 2.0 \times 10^6$ cells/mL and the preparation protocol is described in [28]. Two different alginate weight concentrations have been considered, that is 3 wt% (bio-ink 1) and 2 wt% (bio-ink 2). The corresponding rheological parameters have been obtained by least-squares fittings of rheometry data reported in [28] and obtained via a cone-plate rotational approach. Table 1 summarizes the obtained Carreau–Yasuda rheological parameters (coefficient of determination $R^2 = 0.999$), together with alginate weight concentrations and mass densities. The extruder geometrical parameters adopted for the analyzed case studies (see Fig. 1) are reported in Table 2. In agreement with commercially-available devices [60], nozzle diameters D in the range $0.15 \div 0.51$ mm have been considered. Moreover, different values of the extrusion velocity $\overline{v}$ have been analyzed within the common range of interest for extrusion-based bioprinting processes (6÷24 mm/s, in agreement with [47]).

Section 3.1 present detailed analyses of the entire *in-silico* strategy for bio-ink 1, while for the sake of compactness only the main results obtained for bio-ink 2 are reported in Section 3.2.

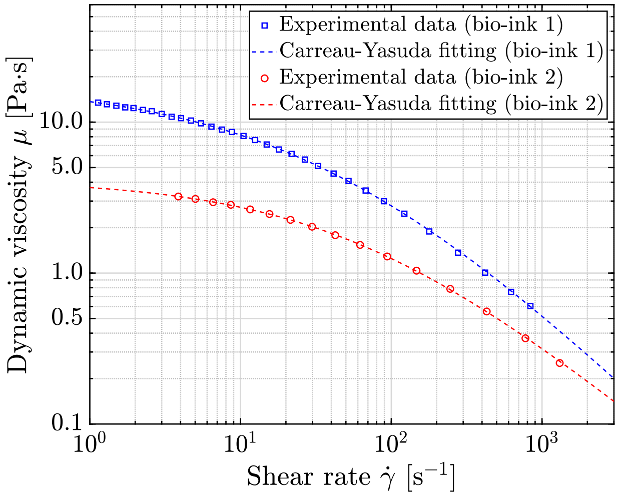

Fig. 4. Dynamic viscosity μ vs. shear rate $\dot{\gamma}$ for the bio-inks employed in numerical applications. Experimental data [28] and least-squares fittings based on the adopted Carreau–Yasuda model ($R^2 = 0.999$).

Table 1
Material properties for the alginate-based bio-inks analyzed in the present work and reported in [28].

Bio-ink	wt [%]	ρ [kg/m^3]	μ_0 [Pa s]	μ_∞ [Pa s]	λ [s]	n [–]	a [–]
1	3	1000	18.190	0.001	0.02453	0	0.5035
2	2	1000	4.176	0.001	0.01560	0.1562	0.5800

Table 2
Geometrical parameters adopted for defining the extruder model (see Fig. 1).

D_{in} [mm]	D' [mm]	L'_c [mm]	$L_c = L'_n$ [mm]	L_n [mm]	D [mm]
2.64	1.98	1.08	1.53	11.9	0.15÷0.51

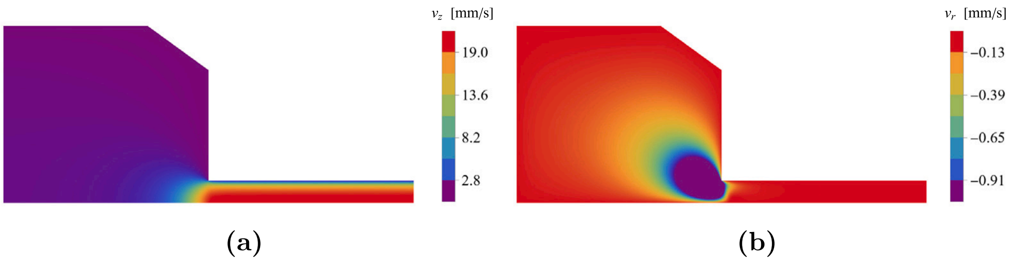

Fig. 5. Case study with bio-ink 1, $D = 0.33$ mm and $\bar{v} = 15$ mm/s. Contour plots of: (a) axial velocity v_z [mm/s]; (b) radial velocity v_r [mm/s].

3.1. Bio-ink 1

3.1.1. CFD simulations

This section analyses typical results obtained from high-fidelity CFD simulations. In particular, the case study with $D = 0.33$ mm and $\bar{v} = 15$ mm/s is reported. Fig. 5 shows the distribution of the axial (v_z) and radial (v_r) velocity components from high-fidelity CFD simulations, and Fig. 6 depicts the computed shear and extensional stress fields. In detail, Figs. 6(a) and 6(b) report shear and extensional stress distributions. Figs. 6(c) and 6(d) show trajectories and stresses experienced by bio-ink particles moving from two different inlet radial positions, identified at 50% and 95% of the inlet radius, respectively. It can be clearly observed that bio-ink particles with starting positions far from the extruder axis are subject to higher shear stresses in the nozzle and higher peaks of extensional stresses, although these latter are significant only in a limited region of the extruder close to the nozzle inlet.

Fig. 7 shows the distribution of the shear rate $\dot{\gamma}$ and the dynamic viscosity μ inside the extruder, highlighting that the highest values of $\dot{\gamma}$ occur near the nozzle wall, where μ assumes the lowest values according to the simulated shear-thinning behavior.

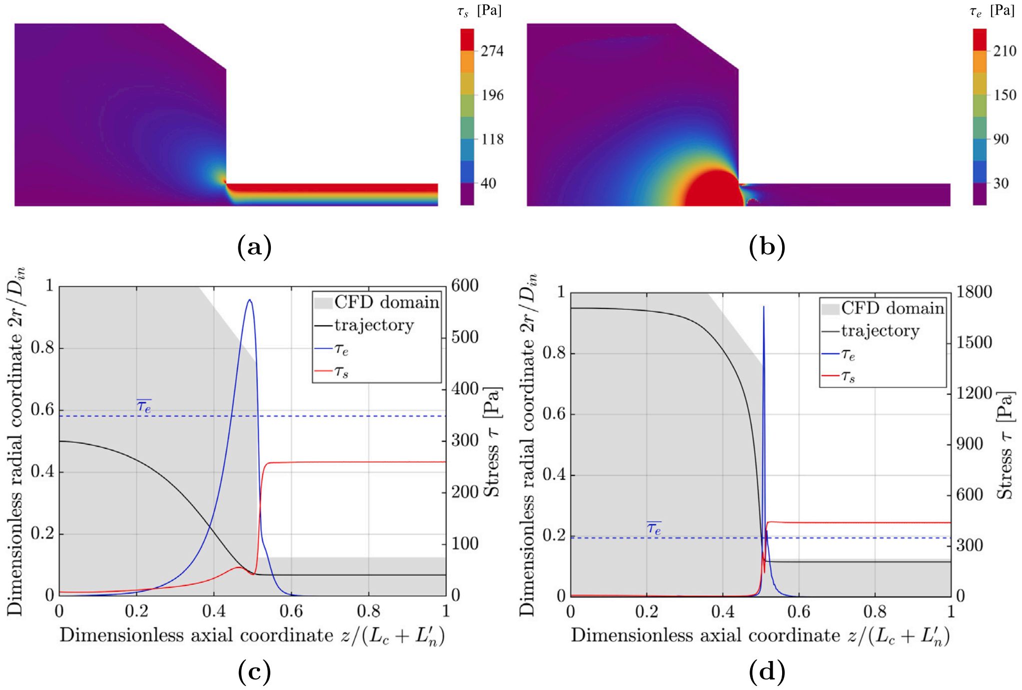

Fig. 6. Case study with bio-ink 1, $D = 0.33$ mm and $\overline{v} = 15$ mm/s. Contour plots of: (a) shear stress τ_s [Pa]; (b) extensional stress τ_e [Pa]. Trajectory and stress experienced by a bio-ink particle starting from a specific inlet radial position: (c) 50% of the inlet radius; (d) 95% of the inlet radius.

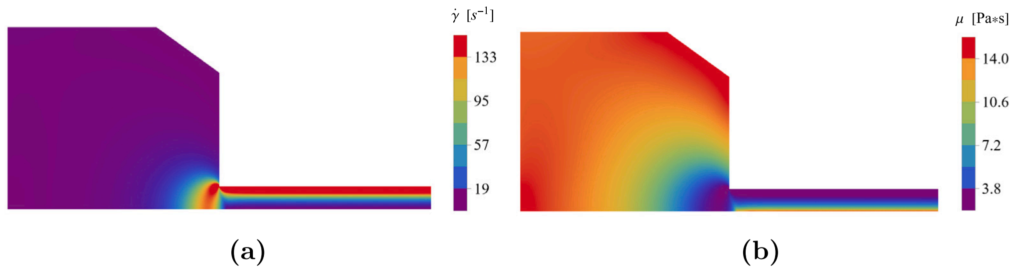

Fig. 7. Case study with bio-ink 1, $D = 0.33$ mm and $\overline{v} = 15$ mm/s. Contour plots of: (a) shear rate $\dot{\gamma}$ [s^{-1}]; (b) dynamic viscosity μ [Pa s].

3.1.2. Cell damage prediction

Soundness and effectiveness of the cell damage model described by Eq. (19) are proven by reproducing some experimental data available in the literature. In detail, starting from the average extensional stress $\overline{\tau}_e$ computed via CFD simulations and by fixing a description for A_{eq} (see Eq. (16)) as depending on the expected damage scenario, experimental data on cell damage are fitted via Eq. (19) through the least-squares method.

Referring to the experimental measurements reported in [28] and associated to the previously-introduced scenario 1 (see Fig. 2), Figs. 8(a) and 9 summarize the obtained fitting results (see Table B.3 in Appendix B for more results). The accuracy of the fitting ($R^2 = 0.964$) demonstrates the effectiveness of proposed damage description. Model parameters resulting from the fitting procedure are reported in Table 3 and are identified as set 1. Correspondingly, Fig. 8(b) depicts extensional stress-induced (d_e), shear stress-induced (d_s) and total cell damage (d) as functions of the extrusion velocity ($\overline{v}$) and for two nozzle geometries ($L_n = 11.9$ mm; $D = 0.33$ mm and $D = 0.51$ mm). It can be observed that when the extrusion velocity $\overline{v}$ increases (or equivalently, when the printing pressure Δp increases), both cell damage portions caused by shear stress in the nozzle and by extensional stress in the contractive region increase. Below a certain threshold value of the extrusion velocity (depending on the nozzle diameter D) the extensional stress-induced cell damage d_e results even higher than the shear stress-induced damage contribution d_s, highlighting the relevance of accounting for extensional effects.

In order to prove the model capability to catch also experimental responses associated to the scenario 2 introduced in Fig. 2, reference is made to experimental evidence discussed in [29]. Model parameters in Eq. (19) are thus identified such to reproduce this new experimental dataset, their values being reported in Table 3 and denoted as set 2. A very effective comparison can be

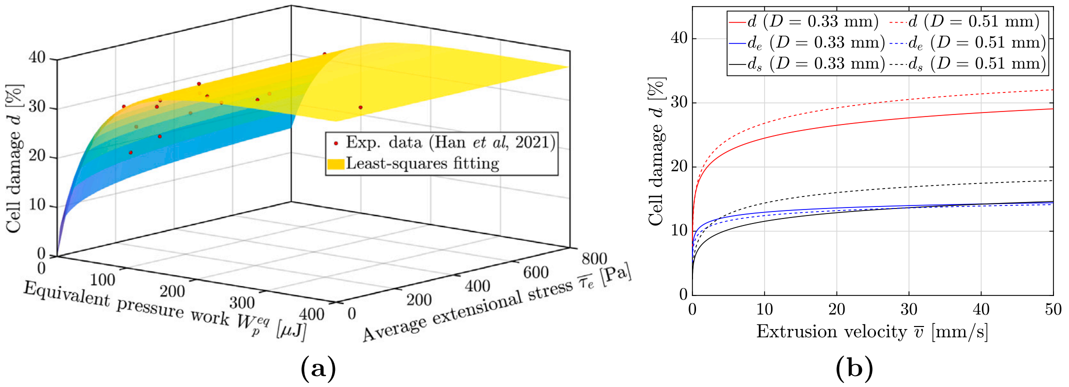

Fig. 8. (a) Fitting of the experimental data reported in [28] (bio-ink 1, human dermal fibroblasts suspended in a 3 wt% alginate-based aqueous solution) via the proposed cell damage model. Corresponding model parameters are summarized in Table 3 (set 1). (b) Extensional stress-induced (d_e), shear stress-induced (d_s) and total cell damage (d) as functions of the extrusion velocity ($\overline{v}$) and for two different values of nozzle diameter D (with $L_n = 11.9$ mm).

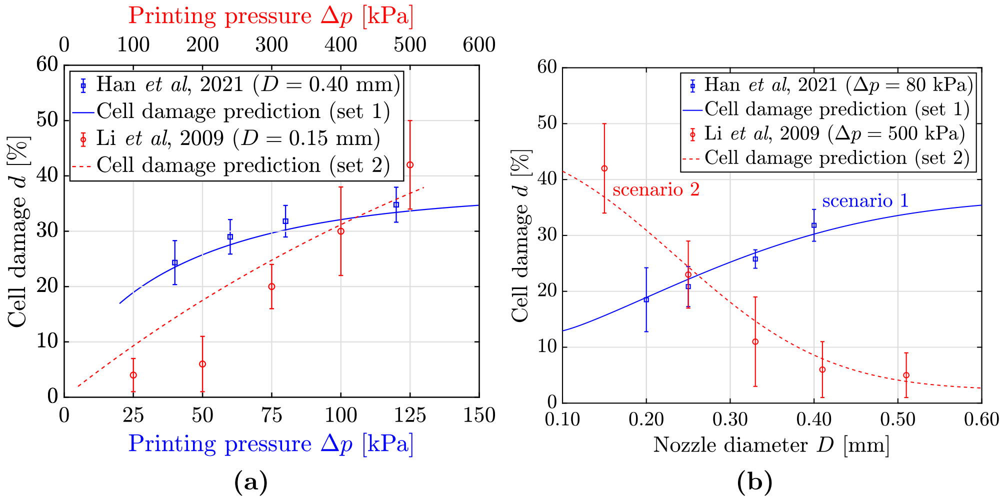

Fig. 9. Comparison of the cell damage predicted via the proposed model with the experimental data (bio-ink 1) provided by Han et al. [28] (scenario 1, blue lines and symbols) and by Li et al. [29] (scenario 2, red lines and symbols). (a) Cell damage d vs. printing pressure Δp for a given value of the nozzle diameter D. (b) Cell damage d vs. nozzle diameter D for a given value of the printing pressure Δp.

Table 3
Values of model parameters adopted for describing experimental scenarios introduced in Fig. 2 via the proposed cell damage model. Set 1 (respectively, set 2) refers to the scenario 1 (resp., scenario 2).

Set	A_0 [mm^2]	$A_{eq,\infty}$ [mm^2]	k_1 [mm^{-2}]	k_2 [mm^{-2}]	a_p [μJ^{-1}]	a_e [Pa$^{-b_e}$]	b_e [–]	$d_{e,max}$ [–]	d_{max} [–]
1	0.50	0.70	0	4	0.0211	0.1752	0.3654	0.1725	0.3681
2	0.0079	$3.7 \cdot 10^{-4}$	0.5	18	0.01	0	0	0	0.80

established, recovering the experimental evidence that, for a fixed value of the printing pressure, cell damage reduces when the nozzle diameter increases (see Fig. 9).

It is noteworthy that experimental measurements in [29] refer to a different bio-ink, whose high viscosity determines significantly higher pressures that typical values adopted in the present work (based on [28]). However, in order to be coherent with the rest of present study, also set 2 of the damage law will be referred in the following to the bio-inks analyzed in [28], and thus to the corresponding range of printing pressures.

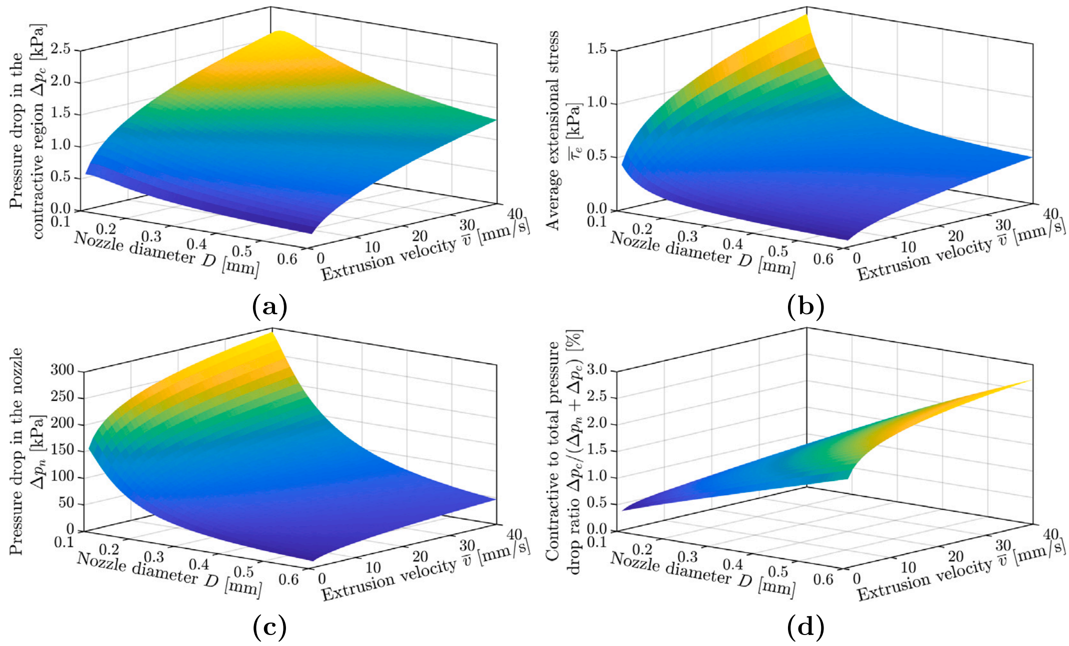

Fig. 10. Surface plots of post-processing quantities computed via the proposed reduced-order model (bio-ink 1): (a) Δp_c, (b) $\overline{\tau}_e$, (c) Δp_n, (d) $\Delta p_c/(\Delta p_n + \Delta p_c)$ vs. nozzle diameter D and extrusion velocity $\overline{v}$.

3.1.3. Calibration and validation of the reduced-order model

The reduced-order model (ROM) introduced in Section 2.4 allows to express quantities Δp_c, $\overline{\tau}_e$ and $\Delta p_n/L_n$ as:

$$\Delta p_c = \frac{\overline{\mu}\,\overline{v}}{D}\left[\alpha_{c,1}\left(\frac{D}{D_{in}}\right)^{\alpha_{c,2}} + \alpha_{c,3}\right]\left(\frac{\rho\overline{v}D}{\overline{\mu}}\right)^{-\left[\beta_{c,1}\left(\frac{D}{D_{in}}\right)^{\beta_{c,2}} + \beta_{c,3}\right]}, \tag{25a}$$

$$\overline{\tau_e} = \frac{\overline{\mu}\,\overline{v}}{D}\left[\alpha_{e,1}\left(\frac{D}{D_{in}}\right)^{\alpha_{e,2}} + \alpha_{e,3}\right]\left(\frac{\rho\overline{v}D}{\overline{\mu}}\right)^{-\left[\beta_{e,1}\left(\frac{D}{D_{in}}\right)^{\beta_{e,2}} + \beta_{e,3}\right]}, \tag{25b}$$

$$\frac{\Delta p_n}{L_n} = \frac{\overline{\mu}\,\overline{v}}{D^2}\left[\alpha_{n,1}\left(\frac{D}{L_n}\right)^{\alpha_{n,2}} + \alpha_{n,3}\right]\left(\frac{\rho\overline{v}D}{\overline{\mu}}\right)^{-\left[\beta_{n,1}\left(\frac{D}{L_n}\right)^{\beta_{n,2}} + \beta_{n,3}\right]}, \tag{25c}$$

where parameters $\alpha_{y,i}$ and $\beta_{y,i}$ (with $y = c, e, n$ and $i = 1, 2, 3$) have been calibrated based on 35 high-fidelity CFD simulations. In particular, 5 values of the nozzle diameter D (i.e., 0.15, 0.25, 0.33, 0.41 and 0.51 mm) and 7 values of the extrusion velocity $\overline{v}$ (i.e., 6, 9, 12, 15, 18, 21 and 24 mm/s) are considered. Moreover, 30 additional simulations are performed to validate the ROM predictions, by setting 5 different values for D (0.20, 0.30, 0.35, 0.45 and 0.55 mm) and 6 for $\overline{v}$ (7.5, 10.5, 13.5, 16.5, 19.5 and 22.5 mm/s). The number of simulations employed for the calibration of the ROM follows a convergence study, where high-fidelity values of post-processing quantities in Eqs. (25) are compared with ROM values. The final mean error with the employed calibration dataset is lower than 2.60% on the validation dataset, thus proving the excellent performance of the proposed approach. For the sake of compactness, more results and details are provided in Appendices A and B, where calibrated parameters are also given (see Table A.2).

In Fig. 10, surface plots of post-processing quantities computed via the proposed reduced-order model are shown, highlighting their dependence on the nozzle diameter D and on the extrusion velocity $\overline{v}$. In detail, it clearly appears that pressure drops within nozzle and contractive regions, as well as the average measure of the extensional stress, tend to increase when the extrusion velocity increases or the nozzle diameter decreases. It is noteworthy that values of extensional stresses are comparable to the ones of shear stresses although the pressure drop in the contractive region is only a minor portion (<3%) of the total printing pressure within the full range of printing conditions for the considered extruder geometry.

3.1.4. Nomograms

Nomograms in the parameters space of nozzle diameter D and printing pressure Δp are shown in Figs. 11 and 12. In particular, Fig. 11 shows the isopleths of mass flow rate $\dot{m}$ and Fig. 12 of cell viability c_v. In both cases, the black dashed lines delimit the calibration area of the reduced-order model (dark gray regions) and they identify curves at a fixed extrusion velocity $\overline{v}$ (namely,

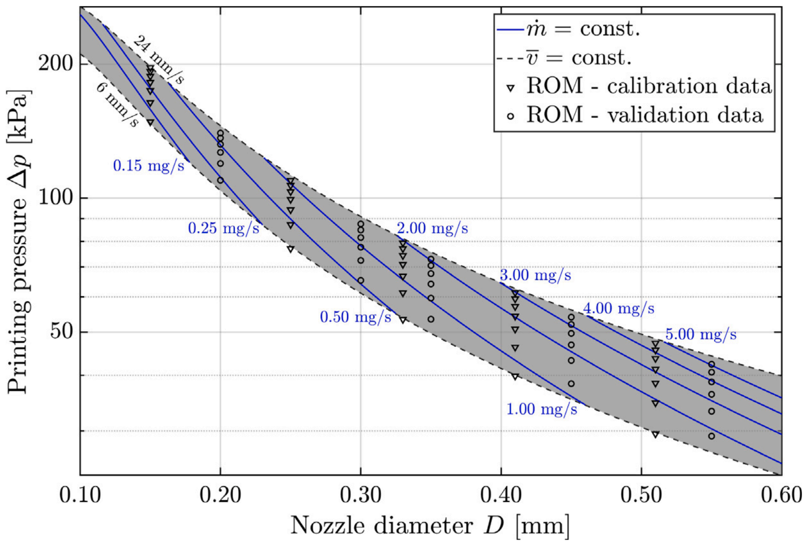

Fig. 11. Nomogram built from the reduced-order model (ROM) by referring to isopleths of mass flow rate $\dot{m}$ in the parameters space (nozzle diameter D, printing pressure Δp) and delimited by limit values of the extrusion velocity $\overline{v}$ (bio-ink 1).

Table 4
Values of model parameters adopted for describing cell damage via the proposed model (bio-ink 2).

A_0 [mm^2]	$A_{eq,\infty}$ [mm^2]	k_1 [mm^{-2}]	k_2 [mm^{-2}]	a_p [μJ^{-1}]	a_e [Pa$^{-b_e}$]	b_e [–]	$d_{e,max}$ [–]	d_{max} [–]
0.50	0.70	0	4	0.0281	0.4977	0.1428	0.2795	0.4358

iso-$\overline{v}$) equal to limit values in the analyzed range. Nomogram in Fig. 11 shows that the lower the nozzle diameter D with the same printing pressure Δp or the lower the printing pressure with the same nozzle diameter, the lower the mass flow rate $\dot{m}$. The complex non-linear relationship between process variables is quantified with such easy-to-use graphical tool. Fig. 11 also reports data adopted for calibrating and validating the reduced-order model (ROM). The mean relative error obtained by computing $\dot{m}$ via the proposed nomogram against the full set of CFD simulations (both calibration and validation dataset) is about 3.5%.

In Fig. 12 two different nomograms for cell viability are proposed, each associated with the two experimental scenarios previously discussed. Isopleths of cell viability c_v exhibit totally different trends, depending on the specific experimental scenario at hand. For the first scenario, Fig. 12(a) also reports the available experimental data in [28] on cell damage within the region of interest (see Table B.3). Remarkably, for this scenario, the graphical computation of cell viability c_v from the nomogram is accurate despite the sparse distribution of experimental data within the parameters space (D, Δp), obtaining a mean relative error of about 1.8%.

3.2. Bio-ink 2

The previously-described analyses have been carried out also by referring to the bio-ink 2 (see Fig. 4). For the sake of compactness, detailed outcomes are reported in Appendices A and B. Also in this case, the proposed reduced-order modeling strategy predicts the quantities under consideration with excellent performance, with average relative error lower than 3.30% with respect to the validation dataset.

3.2.1. Cell damage prediction

The cell damage model proposed in Section 2.2 has been adopted to reproduce the experimental measurements reported in [28] for the bio-ink 2. Fig. 13(a) highlights the effectiveness of the obtained fitting (R^2 = 0.992), associated with model parameters reported in Table 4. Fig. 13(b) depicts extensional stress-induced (d_e), shear stress-induced (d_s) and total cell damage (d) as functions of the extrusion velocity ($\overline{v}$) and for two nozzle geometries ($L_n = 11.9$ mm; $D = 0.33$ mm and $D = 0.51$ mm).

3.2.2. Nomograms

Nomograms associated with the bio-ink 2 are reported in Fig. 14(a), with isopleths of mass flow rate $\dot{m}$, and Fig. 14(b), with isopleths of cell viability c_v. Fig. 14(a) also reports data adopted for calibrating and validating the ROM for the bio-ink 2. The mean relative error obtained by computing $\dot{m}$ via the proposed nomogram against the full set of CFD simulations is about 2.1%. In the same figures, nomograms built for the bio-ink 1 from Section 3.1.4 have been also reported, so as to provide a quick and easy visual comparison between bio-inks with the same cell type but different polymer weight concentrations.

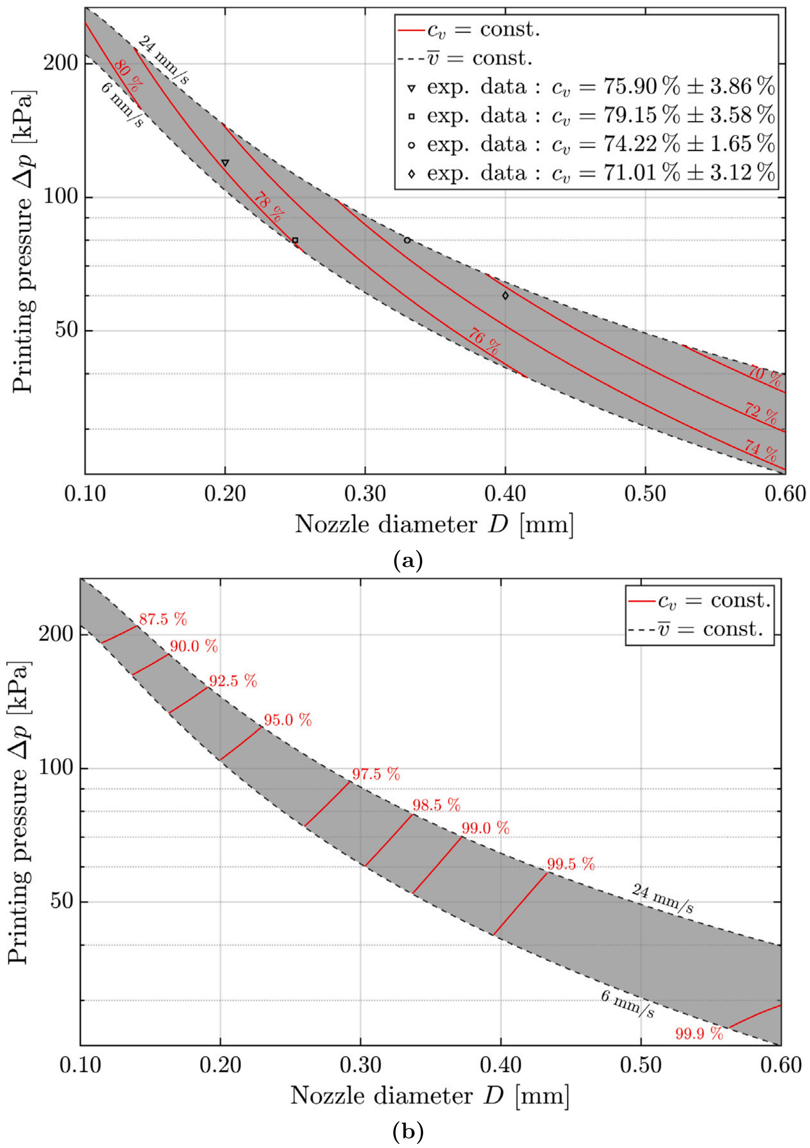

Fig. 12. Nomograms built from the reduced-order model by referring to isopleths of cell viability c_v for: (a) cell damage scenario 1; (b) cell damage scenario 2 (see Section 2.2). Isopleths are reported in the parameters space (nozzle diameter D, printing pressure Δp) and delimited by limit values of the extrusion velocity $\overline{v}$ (bio-ink 1). Experimental data from [28].

4. Concluding remarks

In the planning of bioprinting, the definition of a suitable setting for the fundamental process variables (such as printing pressure, nozzle diameter, target extrusion velocity or mass flow rate, desired cell viability) might be a challenging task, hampered by their strong non-linear coupling.

The present study proposed a novel methodological approach that allows for a more rational and quick definition of suitable target conditions, enabling for an effective bioprinting planning. To this aim a reduced-order model (ROM) able to synthesize the non-linear coupling among fundamental process variables has been proposed. It has been also integrated with a novel cell damage description, specialized to extrusion-based bioprinting procedures and formulated, in agreement with the actual experimental evidence, by consistently generalizing available cell damage approaches.

By referring to a realistic case study, the reduced-order model has been calibrated and validated by means of a limited number of high-fidelity numerical simulations of the bio-ink fluid-dynamics during extrusion. Moreover, a limited number of experimental data has been employed to calibrate the cell damage law. As a result, the proposed framework allowed the construction of bio-ink specific nomograms that can provide fast, useful and effective graphical indications. Isopleths within such nomograms allow, for

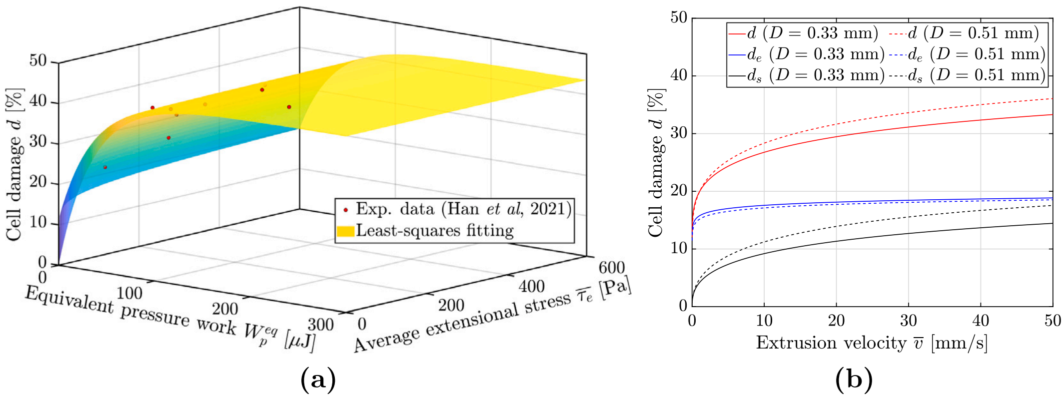

Fig. 13. (a) Fitting of the experimental data reported in [28] (bio-ink 2, human dermal fibroblasts suspended in a 2 wt% alginate-based aqueous solution) via the proposed cell damage model. Corresponding model parameters are summarized in Table 4. (b) Extensional stress-induced (d_e), shear stress-induced (d_s) and total cell damage (d) as functions of the extrusion velocity ($\overline{v}$) and for two different values of nozzle diameter D (bio-ink 2, with $L_n = 11.9$ mm).

instance, to easily obtain how the extrusion velocity, mass flow rate and cell viability vary as functions of nozzle diameter and printing pressure, or otherwise how the printing pressure shall vary when the nozzle diameter is changed but a constant extrusion velocity, mass flow rate or cell viability is desired. Accordingly, the proposed modeling strategy paves the way towards the definition of user-friendly and powerful design tools able to reduce the time-consuming and expensive trial-and-error experimental procedures, actually performed in laboratory practice.

From a methodological point of view, the proposed approach belongs to the context of *in-silico*-based enabling technologies for bioprinting optimization, that are actually gaining a growing interest and remarkable results [17,61]. In addition, the mechanistic rationale behind the proposed strategy is alternative to the black-box perspective of experiment-based design strategies involving artificial intelligence techniques [62]. Nevertheless, the proposed methodological framework could be potentially employed in conjunction with these latter approaches, by allowing to enrich, through simulations and reduced-order models, the experimental datasets required for training surrogate models built via machine learning methods [63].

Clearly, the present study is not exempt from limitations. Firstly, it has been verified only towards alginate-based bio-inks with fixed cell density and two polymer concentrations. Verification towards different bio-ink types and, possibly, generalizations with other rheological laws, would be of high interest. Moreover, future works will focus on the ROM calibration and on the definition of nomograms addressing different bio-inks characterized by different cell types and densities, and/or polymer types. In this context, the study could be also enhanced in order to describe the viscoelastic flow of the bio-ink outside of the nozzle, allowing to possibly account for some post-printing mechanisms. An additional limitation is that the present study addresses only a specific bioprinting technology. Moreover, different geometries of the extrusion system should be investigated, considering also possible non-cylindrical configurations. Furthermore, more knowledge on cell distributions within the nozzles would allow to better verify the concept of effective area introduced in the proposed cell damage law, and would allow for its identification based on a sound mechanistic perspective. To this goal, *ad hoc* experimental measurements or numerical simulations accounting for fluid–structure interaction mechanisms between cells, hydrogel matrix and extruder walls may provide precious information. Finally, authors hope that joint experimental–computational studies in the field may be developed soon, allowing to overcome the gap towards a complete validation of the proposed approach and opening also to further generalizations and enhancements.

Declaration of competing interest

The authors declare that they have no known competing financial interests or personal relationships that could have appeared to influence the work reported in this paper.

Data availability

Data will be made available on request.

Acknowledgments

This work is partially funded by Regione Lazio (POR FESR LAZIO 2014–2020; Progetti di Gruppi di Ricerca 2020; project: BIOPMEAT, n. A0375-2020-36756). Part of this work was carried out with the support from the Italian National Group for Mathematical Physics (GNFM-INdAM).

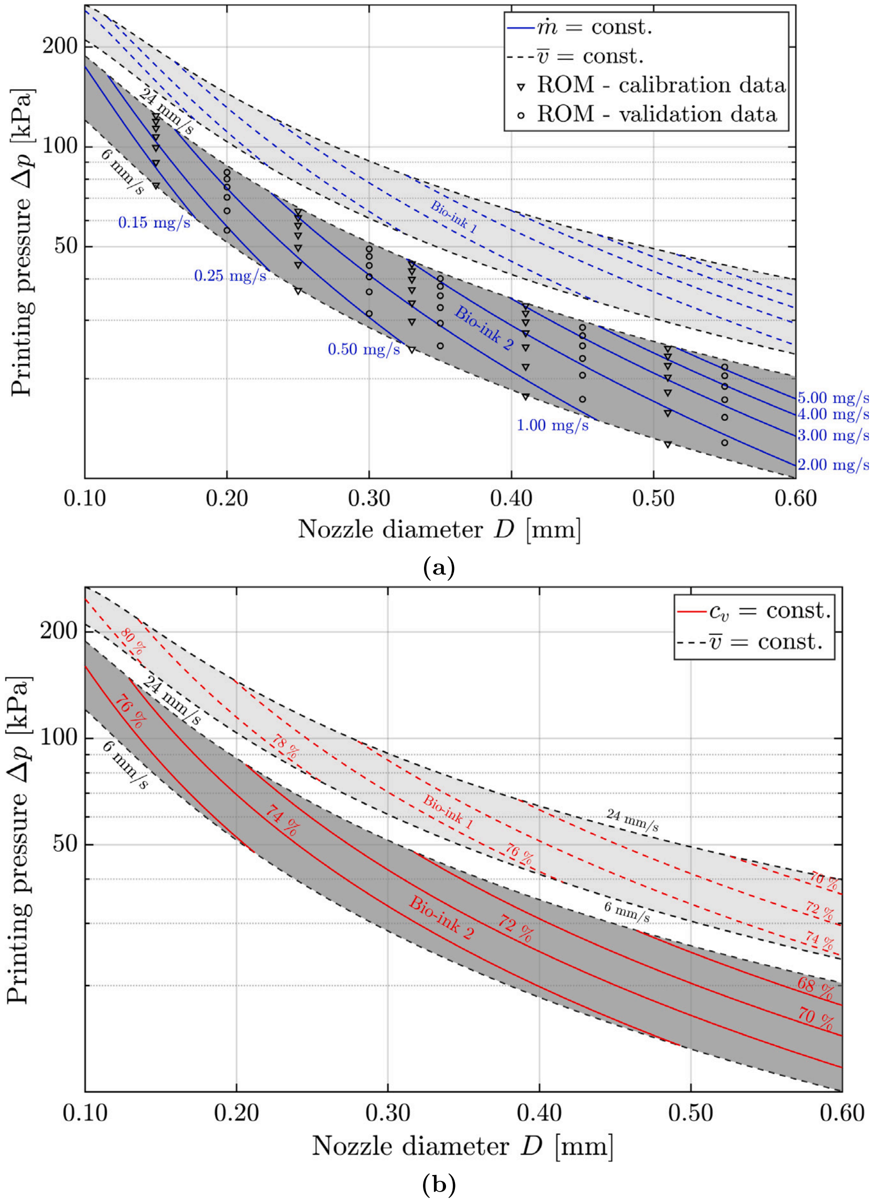

Fig. 14. Nomograms built from the reduced-order model by referring to: (a) isopleths of mass flow rate $\dot{m}$; (b) isopleths of cell viability c_v. Isopleths are reported in the parameters space (nozzle diameter D, printing pressure Δp) and delimited by limit values of the extrusion velocity $\overline{v}$ (bio-ink 2).

Appendix A. Reduced-order modeling procedure

Parameters $\alpha_{y,i}$ and $\beta_{y,i}$ (with $y = c, e, n$ and $i = 1, 2, 3$) defining the reduced-order model introduced in Section 2.4 are determined via the following 2-step calibration procedure:

- At the first, the geometry (i.e., the factor ξ) is considered fixed, while Re is varied by varying $\overline{v}$. For a given value of ξ, optimal values of dimensionless quantities α_y and β_y in Eq. (23) are hence determined by applying the least-squares method to fit the discrete values of functions y obtained from CFD simulations carried out at different values of $\overline{v}$. This calibration stage is repeated for different values of ξ. As a result at the end of this step, discrete values of dimensionless functions α_y and β_y are available for different values of ξ (see Table A.1 for case studies analyzed in this work).
- Results obtained in the previous step are fitted, in turn, via the least-squares method in order to represent functions $\alpha_y(\xi)$ and $\beta_y(\xi)$ via the 2-term power laws introduced in Eqs. (24a) and (24b). As a result, the optimal values of dimensionless parameters $\alpha_{y,i}$ and $\beta_{y,i}$ (with $i = 1, 2, 3$) are determined (see Table A.2 for case studies analyzed in this work).

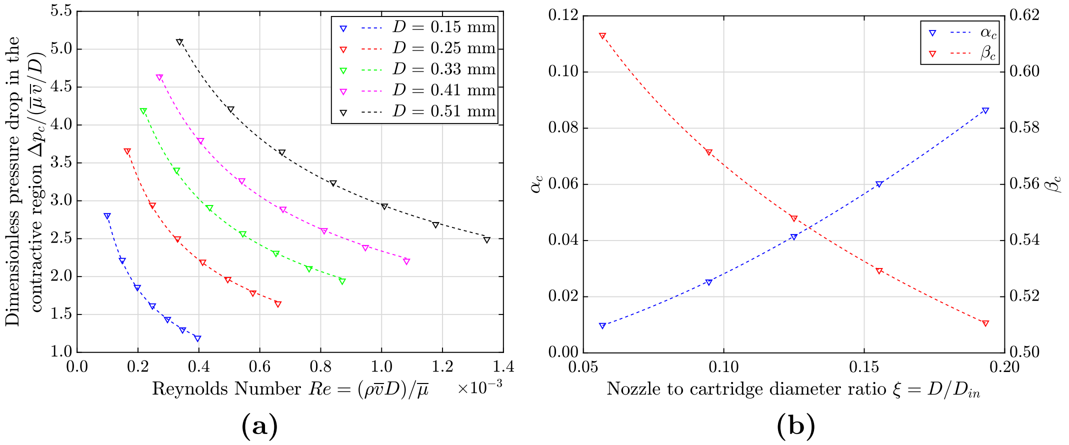

Fig. A.1. ROM calibration for case study with the bio-ink 1. (a) Dimensionless pressure drop along the contractive region Δp_c vs. the Reynolds number Re and for different values of the nozzle diameter D. Comparison between the ROM-based power-law approximation and CFD results (D_{in} = 2.64 mm; L_n = 11.9 mm). Markers: CFD results; dashed line: least-squares fitting (first step of the ROM calibration). (b) Dimensionless functions α_c and β_c vs. $\xi = D/D_{in}$. Markers: results from first step of the ROM calibration; dashed lines: least-squares fitting (second step of the ROM calibration).

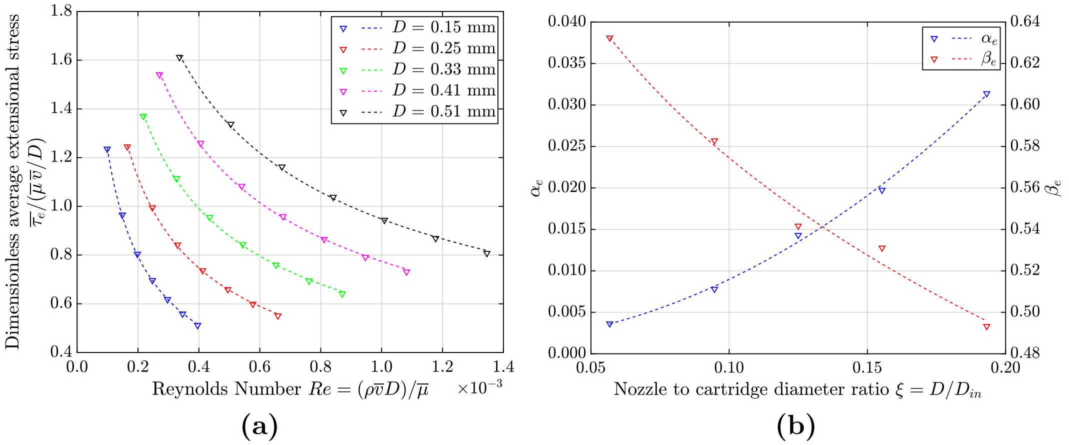

Fig. A.2. ROM calibration for case study with the bio-ink 1.(a) Dimensionless average extensional stress $\overline{\tau_e}$ vs. the Reynolds number Re and for different values of the nozzle diameter D. Comparison between the ROM-based power-law approximation and CFD results (D_{in} = 2.64 mm; L_n = 11.9 mm). Markers: CFD results; dashed line: least-squares fitting (first step of the ROM calibration). (b) Dimensionless functions α_e and β_e vs. $\xi = D/D_{in}$. Markers: results from first step of the ROM calibration; dashed lines: least-squares fitting (second step of the ROM calibration).

Table A.2 reports also the values of maximum and average relative errors computed against the calibration set of CFD results and the validation one, showing the very good performance of the reduced-order model in predicting the quantities under consideration.

For the sake of completeness, the results of the 2-step calibration procedure are illustrated in Figs. A.1 to A.3 for case study with bio-ink 1, where the dimensionless functions of Δp_c, $\overline{\tau}_e$ and $\Delta p_n/L_n$ are plotted versus the Reynolds number Re and for different values of the nozzle diameter D (Figs. A.1(a) to A.3(a)), and where the dimensionless functions $\alpha_y(\xi)$ and $\beta_y(\xi)$ (with $y = c, e, n$) are plotted versus ξ (Figs. A.1(b) to A.3(b)). It is worth observing the excellent accuracy of the functions evaluated via the proposed reduced-order model in comparison with the discrete values resulting from the CFD high-fidelity simulations.

Appendix B. CFD and cell damage results

This Appendix reports detailed numerical outcomes for:

1. the calibration dataset of the ROM, made up by 35 simulations with 5 values of the nozzle diameter D (i.e., 0.15, 0.25, 0.33, 0.41 and 0.51 mm) and 7 values of the extrusion velocity $\overline{v}$ (i.e., 6, 9, 12, 15, 18, 21 and 24 mm/s). Outcomes for the bio-ink 1 are given in Table B.1, while for the bio-ink 2 in Table B.4;
2. the validation dataset of the ROM, made up by 30 additional simulations with 5 different values for D (0.20, 0.30, 0.35, 0.45 and 0.55 mm) and 6 for $\overline{v}$ (7.5, 10.5, 13.5, 16.5, 19.5 and 22.5 mm/s). Outcomes for the bio-ink 1 are given in Table B.2, while for the bio-ink 2 in Table B.5.

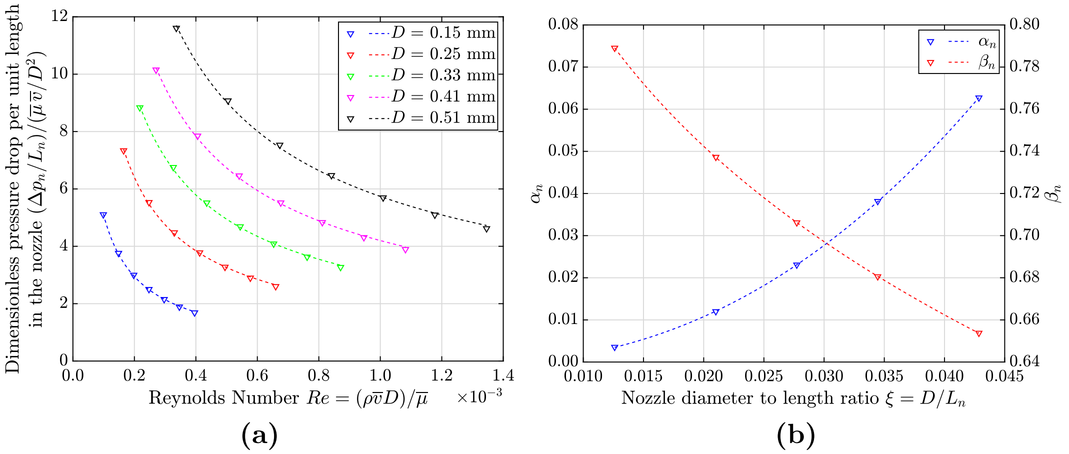

Fig. A.3. ROM calibration for case study with the bio-ink 1. (a) Dimensionless pressure drop per unit length in the nozzle $\Delta p_n/L_n$ vs. the Reynolds number Re and for different values of the nozzle diameter D. Comparison between the ROM-based power-law approximation and CFD results (D_{in} = 2.64 mm; L_n = 11.9 mm). Markers: CFD results; dashed line: least-squares fitting (first step of the ROM calibration). (b) Dimensionless functions α_c and β_c vs. $\xi = D/L_n$. Markers: results from first step of the ROM calibration; dashed lines: least-squares fitting (second step of the ROM calibration).

Table A.1
Values of dimensionless functions $\alpha_y(\xi)$ and $\beta_y(\xi)$ (with $y = c, e, n$) defining the reduced-order model introduced in Section 2.4, and obtained via the first fitting step at different values of ξ and within the considered range of the extrusion velocity $\bar{v}$ (namely, 6÷24 mm/s). D_{in} = 2.64 mm; L_n = 11.9 mm.

	D [mm]				
	0.15	0.25	0.33	0.41	0.51
	Bio-ink 1				
α_c	0.0099	0.0253	0.0415	0.0603	0.0865
β_c	0.6131	0.5717	0.5481	0.5294	0.5108
α_e	0.0036	0.0078	0.0143	0.0197	0.0314
β_e	0.6325	0.5829	0.5417	0.5311	0.4933
α_n	0.0036	0.0120	0.0231	0.0382	0.0627
β_n	0.7891	0.7373	0.7062	0.6806	0.6538
	Bio-ink 2				
α_c	0.1025	0.2254	0.3393	0.4614	0.6202
β_c	0.5107	0.4668	0.4417	0.4217	0.4016
α_e	0.0366	0.0680	0.1054	0.1431	0.1933
β_e	0.5397	0.4868	0.4506	0.4350	0.4047
α_n	0.0780	0.2071	0.3481	0.5177	0.7639
β_n	0.6452	0.5957	0.5657	0.5410	0.5152

Table A.2
Values of model parameters defining the proposed reduced-order model and computed via a 2-step least-squares fitting procedure. Values of maximum ($\mathrm{err}_{\max}$) and average ($\overline{\mathrm{err}}$) relative error against both calibration and validation CFD results are also indicated.

	Model parameters						Calibration		Validation	
	$\alpha_{y,1}$	$\alpha_{y,2}$	$\alpha_{y,3}$	$\beta_{y,1}$	$\beta_{y,2}$	$\beta_{y,3}$	$\mathrm{err}_{\max}$	$\overline{\mathrm{err}}$	$\mathrm{err}_{\max}$	$\overline{\mathrm{err}}$
	Bio-ink 1									
Δp_c	1.2800	1.6209	−0.0025	−1.3758	0.0716	1.7337	2.29%	0.88%	2.10%	0.71%
$\overline{\tau_e}$	0.8683	2.0453	0.0012	−0.7837	0.2491	1.0162	3.83%	1.49%	8.76%	2.59%
$\frac{\Delta p_n}{L_n}$	80.6331	2.2704	−0.0004	−1.1407	0.2278	1.2104	2.76%	1.12%	2.18%	0.86%
	Bio-ink 2									
Δp_c	5.5315	1.3007	−0.0308	−1.1950	0.0918	1.4290	2.10%	0.81%	1.97%	0.69%
$\overline{\tau_e}$	2.1447	1.4751	0.0044	−1.8408	0.0695	2.0482	4.60%	2.33%	10.90%	3.29%
$\frac{\Delta p_n}{L_n}$	200.3455	1.7627	−0.0127	−1.0897	0.2388	1.0287	2.49%	0.99%	2.06%	0.82%

The results from additional simulations performed to calibrate the damage model are also reported in Table B.3 for the bio-ink 1 and in Table B.6 for the bio-ink 2.

Table B.1
Numerical results obtained by 35 high-fidelity CFD simulations employed for the calibration of the proposed reduced-order model (bio-ink 1).

Data		CFD results		
D [mm]	$\overline{v}$ [mm/s]	Δp_c [kPa]	$\overline{\tau_e}$ [kPa]	$\frac{\Delta p_n}{L_n}$ [kPa/mm]
0.15	6	1.02	0.45	12.39
	9	1.21	0.53	13.69
	12	1.35	0.59	14.55
	15	1.47	0.63	15.17
	18	1.57	0.67	15.66
	21	1.66	0.71	16.05
	24	1.73	0.75	16.37
0.25	6	0.80	0.27	6.41
	9	0.96	0.33	7.25
	12	1.09	0.37	7.82
	15	1.20	0.40	8.25
	18	1.29	0.43	8.59
	21	1.37	0.46	8.86
	24	1.43	0.48	9.09
0.33	6	0.69	0.23	4.43
	9	0.85	0.28	5.08
	12	0.96	0.32	5.53
	15	1.06	0.35	5.87
	18	1.15	0.38	6.15
	21	1.22	0.40	6.37
	24	1.29	0.42	6.56
0.41	6	0.62	0.21	3.30
	9	0.76	0.25	3.82
	12	0.87	0.29	4.19
	15	0.96	0.32	4.48
	18	1.04	0.35	4.71
	21	1.11	0.37	4.90
	24	1.17	0.39	5.06
0.51	6	0.55	0.17	2.44
	9	0.68	0.21	2.86
	12	0.78	0.25	3.16
	15	0.87	0.28	3.40
	18	0.94	0.30	3.58
	21	1.01	0.33	3.74
	24	1.07	0.35	3.88

Table B.2
Numerical results obtained by 30 high-fidelity CFD simulations employed for the validation of the proposed reduced-order model (bio-ink 1).

Data		CFD results		
D [mm]	$\overline{v}$ [mm/s]	Δp_c [kPa]	$\overline{\tau_e}$ [kPa]	$\frac{\Delta p_n}{L_n}$ [kPa/mm]
0.20	7.5	0.98	0.34	9.13
	10.5	1.14	0.39	9.96
	13.5	1.26	0.43	10.55
	16.5	1.36	0.47	10.99
	19.5	1.45	0.50	11.35
	22.5	1.52	0.52	11.64
0.30	7.5	0.81	0.27	5.42
	10.5	0.95	0.31	6.01
	13.5	1.06	0.35	6.43
	16.5	1.15	0.38	6.76
	19.5	1.23	0.41	7.02
	22.5	1.30	0.44	7.24
0.35	7.5	0.75	0.25	4.43
	10.5	0.88	0.29	4.94
	13.5	0.99	0.33	5.31
	16.5	1.08	0.36	5.60
	19.5	1.15	0.38	5.83
	22.5	1.22	0.41	6.03

(*continued on next page*)

Table B.2 (*continued*).

Data		CFD results		
D [mm]	$\overline{v}$ [mm/s]	Δp_c [kPa]	$\overline{\tau_e}$ [kPa]	$\frac{\Delta p_n}{L_n}$ [kPa/mm]
0.45	7.5	0.66	0.22	3.16
	10.5	0.78	0.26	3.56
	13.5	0.88	0.29	3.86
	16.5	0.96	0.32	4.09
	19.5	1.03	0.34	4.29
	22.5	1.10	0.37	4.45
0.55	7.5	0.59	0.19	2.40
	10.5	0.70	0.23	2.73
	13.5	0.79	0.26	2.98
	16.5	0.87	0.29	3.17
	19.5	0.94	0.31	3.34
	22.5	1.00	0.33	3.47

Table B.3
Cell damage prediction in comparison with the experimental measurements (bio-ink 1) proposed in [28], for different nozzle geometries. Experimental data are expressed in terms of the average cell damage ($\overline{d}_{exp}$) and the corresponding standard deviation (SD).

Operating parameters			Computed quantities			Exp. data [28]
D [mm]	L_n [mm]	Δp [kPa]	W_p^{eq} [μJ]	$\overline{\tau_e}$ [Pa]	d [%]	$\overline{d}_{exp} \pm SD$ [%]
0.20	11.9	80	14.95	215.74	18.90	18.50 ± 5.72
		120	22.43	402.53	22.39	24.10 ± 3.86
0.25		80	23.37	295.42	22.16	20.85 ± 3.58
		120	35.05	642.31	25.94	25.00 ± 1.61
0.33		80	40.71	464.72	26.89	25.78 ± 1.65
0.40		40	29.91	199.17	23.50	24.33 ± 3.97
		60	44.86	380.65	27.55	28.99 ± 3.12
		80	59.82	771.81	30.24	31.81 ± 2.85
	25.4	40	63.84	76.26	29.63	30.94 ± 4.98
		60	95.76	124.19	33.32	32.20 ± 5.23
		80	127.67	180.54	35.08	35.64 ± 5.72
	50.8	40	127.67	36.66	34.79	32.95 ± 1.26
		60	191.51	56.62	36.31	36.30 ± 1.81
		80	255.35	76.26	36.68	36.79 ± 3.02
		120	383.02	124.19	36.80	37.60 ± 2.74

Table B.4
Numerical results obtained by 35 high-fidelity CFD simulations employed for the calibration of the proposed reduced-order model (bio-ink 2).

Data		CFD results		
D [mm]	$\overline{v}$ [mm/s]	Δp_c [kPa]	$\overline{\tau_e}$ [kPa]	$\frac{\Delta p_n}{L_n}$ [kPa/mm]
0.15	6	0.45	0.20	6.41
	9	0.55	0.24	7.51
	12	0.63	0.28	8.32
	15	0.71	0.31	8.97
	18	0.77	0.33	9.50
	21	0.82	0.35	9.96
	24	0.87	0.37	10.37
0.25	6	0.33	0.11	3.07
	9	0.41	0.14	3.68
	12	0.48	0.17	4.14
	15	0.54	0.19	4.51
	18	0.60	0.20	4.82
	21	0.64	0.22	5.09
	24	0.68	0.23	5.32
0.33	6	0.28	0.09	2.04
	9	0.35	0.12	2.48
	12	0.41	0.14	2.81

(*continued on next page*)

Table B.4 (*continued*).

Data		CFD results		
D [mm]	$\overline{v}$ [mm/s]	Δp_c [kPa]	$\overline{\tau_e}$ [kPa]	$\frac{\Delta p_n}{L_n}$ [kPa/mm]
	15	0.47	0.15	3.08
	18	0.52	0.17	3.31
	21	0.56	0.18	3.51
	24	0.60	0.19	3.68
0.41	6	0.24	0.08	1.47
	9	0.31	0.10	1.81
	12	0.37	0.12	2.06
	15	0.41	0.14	2.28
	18	0.46	0.15	2.45
	21	0.50	0.17	2.61
	24	0.53	0.18	2.75
0.51	6	0.21	0.07	1.05
	9	0.27	0.09	1.31
	12	0.32	0.10	1.51
	15	0.36	0.12	1.67
	18	0.40	0.13	1.81
	21	0.44	0.14	1.93
	24	0.47	0.15	2.04

Table B.5
Numerical results obtained by 30 high-fidelity CFD simulations employed for the validation of the proposed reduced-order model (bio-ink 2).

Data		CFD results		
D [mm]	$\overline{v}$ [mm/s]	Δp_c [kPa]	$\overline{\tau_e}$ [kPa]	$\frac{\Delta p_n}{L_n}$ [kPa/mm]
0.20	7.5	0.43	0.15	4.68
	10.5	0.51	0.17	5.35
	13.5	0.58	0.20	5.88
	16.5	0.64	0.22	6.31
	19.5	0.69	0.23	6.67
	22.5	0.74	0.25	6.99
0.30	7.5	0.34	0.11	2.62
	10.5	0.41	0.14	3.04
	13.5	0.47	0.16	3.37
	16.5	0.52	0.17	3.65
	19.5	0.56	0.19	3.88
	22.5	0.61	0.20	4.09
0.35	7.5	0.31	0.10	2.09
	10.5	0.37	0.12	2.44
	13.5	0.43	0.14	2.72
	16.5	0.48	0.16	2.95
	19.5	0.52	0.17	3.15
	22.5	0.56	0.18	3.32
0.45	7.5	0.26	0.09	1.44
	10.5	0.32	0.10	1.70
	13.5	0.37	0.12	1.90
	16.5	0.41	0.14	2.08
	19.5	0.45	0.15	2.23
	22.5	0.49	0.16	2.36
0.55	7.5	0.23	0.08	1.06
	10.5	0.28	0.09	1.26
	13.5	0.33	0.11	1.43
	16.5	0.37	0.12	1.56
	19.5	0.40	0.13	1.68
	22.5	0.44	0.14	1.79

Table B.6
Cell damage prediction in comparison with the experimental measurements (bio-ink 2) proposed in [28], for different nozzle geometries. Experimental data are expressed in terms of the average cell damage ($\overline{d}_{exp}$) and the corresponding standard deviation (SD).

Operating parameters			Computed quantities			Exp. data [28]
D [mm]	L_n [mm]	Δp [kPa]	W_p^{eq} [μJ]	$\overline{\tau}_e$ [Pa]	d [%]	$\overline{d}_{exp} \pm SD$ [%]
0.20	11.9	40	7.48	97.76	22.21	22.31 ± 2.04
		80	14.95	238.15	27.11	26.61 ± 4.00
0.40		40	29.91	222.17	32.71	33.27 ± 2.04
		60	44.86	406.76	36.69	36.90 ± 2.69
	25.4	40	63.84	81.74	39.14	39.55 ± 3.87
		60	95.76	136.57	41.82	40.35 ± 2.63
		80	127.67	202.34	42.88	43.68 ± 0.94
	38.1	40	95.76	51.09	41.72	41.18 ± 4.55
		80	191.51	117.40	43.46	43.91 ± 4.86

References

[1] S. Murphy, A. Atala, 3D bioprinting of tissues and organs, Nat. Biotechnol. 32 (2014) 773–785, http://dx.doi.org/10.1038/nbt.2958.

[2] I.T. Ozbolat, M. Hospodiuk, Current advances and future perspectives in extrusion-based bioprinting, Biomaterials 76 (2016) 321–343, http://dx.doi.org/10.1016/j.biomaterials.2015.10.076.

[3] S. Rahmani Dabbagh, M. Rezapour Sarabi, M.T. Birtek, N. Mustafaoglu, Y.S. Zhang, S. Tasoglu, 3D bioprinted organ-on-chips, Aggregate 4 (2023) e197, http://dx.doi.org/10.1002/agt2.197.

[4] P. Fisch, N. Broguiere, S. Finkielsztein, T. Linder, M. Zenobi-Wong, Bioprinting of cartilaginous auricular constructs utilizing an enzymatically crosslinkable bioink, Adv. Funct. Mater. 31 (2021) 2008261, http://dx.doi.org/10.1002/adfm.202008261.

[5] F. Cadamuro, L. Marongiu, M. Marino, N. Tamini, L. Nespoli, N. Zucchini, A. Terzi, D. Altamura, Z. Gao, C. Giannini, G. Bindi, A. Smith, F. Magni, S. Bertini, F. Granucci, F. Nicotra, L. Russo, 3D bioprinted colorectal cancer models based on hyaluronic acid and signalling glycans, Carbohydr. Polymers 302 (2023) 120395, http://dx.doi.org/10.1016/j.carbpol.2022.120395.

[6] E. Bari, G.M. Di Gravina, F. Scocozza, S. Perteghella, B. Frongia, S. Tengattini, L. Segale, M.L. Torre, M. Conti, Silk fibroin bioink for 3D printing in tissue regeneration: Controlled release of MSC extracellular vesicles, Pharmaceutics 15 (2023) 383, http://dx.doi.org/10.3390/pharmaceutics15020383.

[7] I. Chiesa, C.D. Maria, A. Lapomarda, G.M. Fortunato, F. Montemurro, R.D. Gesù, R.S. Tuan, G. Vozzi, R. Gottardi, Endothelial cells support osteogenesis in an in vitro vascularized bone model developed by 3D bioprinting, Biofabrication 12 (2020) 025013, http://dx.doi.org/10.1088/1758-5090/ab6a1d.

[8] E. Fornetti, F.D. Paolis, C. Fuoco, S. Bernardini, S.M. Giannitelli, A. Rainer, D. Seliktar, F. Magdinier, J. Baldi, R. Biagini, S. Cannata, S. Testa, C. Gargioli, A novel extrusion-based 3D bioprinting system for skeletal muscle tissue engineering, Biofabrication 15 (2023) 025009, http://dx.doi.org/10.1088/1758-5090/acb573.

[9] Y.S. Zhang, G. Haghiashtiani, T. Hübscher, D. Kelly, J.M. Lee, M. Lutolf, M. McAlpine, W.Y. Yeong, M. Zenobi, J. Malda, 3D extrusion bioprinting, Nat. Rev. Dis. Primers 1 (2021) 75, http://dx.doi.org/10.1038/s43586-021-00073-8.

[10] X. Cui, J. Li, Y. Hartanto, M. Durham, J. Tang, H. Zhang, G. Hooper, K. Lim, T. Woodfield, Advances in extrusion 3D bioprinting: A focus on multicomponent hydrogel-based bioinks, Adv. Healthcare Mater. 9 (2020) 1901648, http://dx.doi.org/10.1002/adhm.201901648.

[11] E. Monaldo, H. Hille, L. De Lorenzis, Modelling of extrusion-based bioprinting via floating isogeometric analysis (FLIGA), in: P. Fuschi, A.A. Pisano (Eds.), Book of Abstracts GIMC GMA GBMA 2023, Edizioni Centro Stampa di Ateneo - Università degli Studi di Reggio Calabria "Mediterranea", Reggio Calabria (Italy), ISBN: 978-88-99352-95-0, 2023, pp. 84–85.

[12] M. Hospodiuk, M. Dey, D.M. Sosnoski, I.T. Ozbolat, The bioink: A comprehensive review on bioprintable materials, Biotechnol. Adv. 35 (2017) 217–239, http://dx.doi.org/10.1016/j.biotechadv.2016.12.006.

[13] S. Boularaoui, G. Hussein, K. Khan, N. Christoforou, C. Stefanini, An overview of extrusion-based bioprinting with a focus on induced shear stress and its effect on cell viability, Bioprinting 20 (2020) e00093, http://dx.doi.org/10.1016/j.bprint.2020.e00093.

[14] W. Sun, B. Starly, A.C. Daly, J.A. Burdick, J. Groll, G. Skeldon, W. Shu, Y. Sakai, M. Shinohara, M. Nishikawa, J. Jang, D.-W. Cho, M. Nie, S. Takeuchi, S. Ostrovidov, A. Khademhosseini, R.D. Kamm, V. Mironov, L. Moroni, I.T. Ozbolat, The bioprinting roadmap, Biofabrication 12 (2020) 022002, http://dx.doi.org/10.1088/1758-5090/ab5158.

[15] E. Reina-Romo, S. Mandal, P. Amorim, V. Bloemen, E. Ferraris, L. Geris, Towards the experimentally-informed in silico nozzle design optimization for extrusion-based bioprinting of shear-thinning hydrogels, Front. Bioeng. Biotechnol. 9 (2021) 701778, http://dx.doi.org/10.3389/fbioe.2021.701778.

[16] L. Moroni, T. Boland, J.A. Burdick, C. De Maria, B. Derby, G. Forgacs, J. Groll, Q. Li, J. Malda, V.A. Mironov, C. Mota, M. Nakamura, W. Shu, S. Takeuchi, T.B. Woodfield, T. Xu, J.J. Yoo, G. Vozzi, Biofabrication: A guide to technology and terminology, Trends Biotechnol. 36 (2018) 384–402, http://dx.doi.org/10.1016/j.tibtech.2017.10.015.

[17] A.F. Bonatti, I. Chiesa, G. Vozzi, C. De Maria, Open-source CAD-CAM simulator of the extrusion-based bioprinting process, Bioprinting 24 (2021) e00172, http://dx.doi.org/10.1016/j.bprint.2021.e00172.

[18] A. Dababneh, I. Ozbolat, Bioprinting technology: A current state-of-the-art review, ASME J. Manuf. Sci. Eng. 136 (2014) 061016, http://dx.doi.org/10.1115/1.4028512.

[19] G. Loi, G. Stucchi, F. Scocozza, L. Cansolino, F. Cadamuro, E. Delgrosso, F. Riva, C. Ferrari, L. Russo, M. Conti, Characterization of a bioink combining extracellular matrix-like hydrogel with osteosarcoma cells: Preliminary results, Gels 9 (2023) 129, http://dx.doi.org/10.3390/gels9020129.

[20] A.C. Daly, M.E. Prendergast, A.J. Hughes, J.A. Burdick, Bioprinting for the biologist, Cell 184 (2021) 18–32, http://dx.doi.org/10.1016/j.cell.2020.12.002.

[21] F. Chirianni, G. Vairo, M. Marino, An in-silico approach for process design in extrusion-based bioprinting, in: P. Fuschi, A.A. Pisano (Eds.), Book of Abstracts GIMC GMA GBMA 2023, Edizioni Centro Stampa di Ateneo - Università degli Studi di Reggio Calabria "Mediterranea", Reggio Calabria (Italy), ISBN: 978-88-99352-95-0, 2023, pp. 114–115.

[22] F. Chirianni, G. Vairo, M. Marino, Process design in extrusion-based bioprinting, in: A. Ramos, C. Furtado, A. Colaço, A. Arteiro, A. Furtado, C. Horas, I. Lopes, R. Carvalho, S. Pereira (Eds.), Proceedings of the 7th ECCOMAS Young Investigators Conference (ECCOMAS YIC 2023), Zenodo, 2023, pp. 191–192, http://dx.doi.org/10.5281/zenodo.8393048.

[23] J. Emmermacher, D. Spura, J. Cziommer, D. Kilian, T. Wollborn, U. Fritsching, J. Steingroewer, T. Walther, M. Gelinsky, A. Lode, Engineering considerations on extrusion-based bioprinting: interactions of material behavior, mechanical forces and cells in the printing needle, Biofabrication 12 (2020) 025022, http://dx.doi.org/10.1088/1758-5090/ab7553.

[24] S. Müller, E. Mirzahossein, E. Iftekhar, C. Bächer, S. Schrüfer, D. Schubert, B. Fabry, S. Gekle, Flow and hydrodynamic shear stress inside a printing needle during biofabrication, PLoS One 15 (2020) e0236371, http://dx.doi.org/10.1371/journal.pone.0236371.

[25] X.Y. Tian, M.G. Li, X.B. Chen, Bio-rapid-prototyping of tissue engineering scaffolds and the process-induced cell damage, J. Biomim. Biomater. Biomed. Eng. 17 (2013) 1–23, http://dx.doi.org/10.4028/www.scientific.net/JBBTE.17.1.

[26] X. Chen, M. Li, H. Ke, Modeling of the flow rate in the dispensing-based process for fabricating tissue scaffolds, ASME J. Manuf. Sci. Eng. 130 (2008) 021003, http://dx.doi.org/10.1115/1.2789725.

[27] L. Ning, N. Betancourt, D.J. Schreyer, X. Chen, Characterization of cell damage and proliferative ability during and after bioprinting, ACS Biomater. Sci. Eng. 4 (2018) 3906–3918, http://dx.doi.org/10.1021/acsbiomaterials.8b00714.

[28] S. Han, C.M. Kim, S. Jin, T.Y. Kim, Study of the process-induced cell damage in forced extrusion bioprinting, Biofabrication 13 (2021) 035048, http://dx.doi.org/10.1088/1758-5090/ac0415.

[29] M. Li, X. Tian, N. Zhu, D. Schreyer, X. Chen, Modeling process-induced cell damage in the biodispensing process, Tissue Eng. C 16 (2009) 533–542, http://dx.doi.org/10.1089/ten.TEC.2009.0178.

[30] L. Ning, B. Yang, F. Mohabatpour, N. Betancourt, M. Sarker, P. Papagerakis, D. Chen, Process-induced cell damage: pneumatic vs. screw-driven bioprinting, Biofabrication 12 (2019) 025011, http://dx.doi.org/10.1088/1758-5090/ab5f53.

[31] J. Yang, Y. Dai, J. Li, A different extensional viscosity prediction based on entry pressure drop, J. Appl. Polym. Sci. 131 (2014) 40563, http://dx.doi.org/10.1002/app.40563.

[32] M. Conti, G. Santesarti, F. Scocozza, M. Marino, Chapter 6 - models and simulations as enabling technologies for bioprinting process design, in: M. Conti, M. Marino (Eds.), Bioprinting: From Multidisciplinary Design To Emerging Opportunities, Academic Press, London (United Kingdom), 2022, pp. 137–206, http://dx.doi.org/10.1016/B978-0-323-85430-6.00009-1.

[33] M. Li, X. Tian, D. Schreyer, X. Chen, Effect of needle geometry on flow rate and cell damage in the dispensing-based biofabrication process, Biotechnol. Prog. 27 (2011) 1777–1784, http://dx.doi.org/10.1002/btpr.679.

[34] K. Nair, M. Gandhi, S. Khalil, K. Yan, M. Marcolongo, K. Barbee, W. Sun, Characterization of cell viability during bioprinting process, Biotechnol. J. 4 (2009) 1168–1177, http://dx.doi.org/10.1002/biot.200900004.

[35] R. Chang, J. Nam, W. Sun, Effects of dispensing pressure and nozzle diameter on cell survival from solid freeform fabrication–based direct cell writing, Tissue Eng. A 14 (2008) 41–48, http://dx.doi.org/10.1089/ten.a.2007.0004.

[36] J. Leppiniemi, P. Lahtinen, A. Paajanen, R. Mahlberg, S. Metsä-Kortelainen, T. Pinomaa, H. Pajari, I. Vikholm-Lundin, P. Pursula, V.P. Hytönen, 3D-printable bioactivated nanocellulose–alginate hydrogels, ACS Appl. Mater. Interfaces 9 (26) (2017) 21959–21970, http://dx.doi.org/10.1021/acsami.7b02756.

[37] G.K. Batchelor, An Introduction to Fluid Dynamics, Cambridge University Press, Cambridge UK, 2000, http://dx.doi.org/10.1017/CBO9780511800955.

[38] R.B. Bird, R. Armstrong, O. Hassager, Dynamics of Polymeric Liquids, Vol. 1: Fluid Mechanics, second ed., Wiley, United States of America, 1987.

[39] M. Gallagher, R. Wain, S. Dari, J. Whitty, D. Smith, Non-identifiability of parameters for a class of shear-thinning rheological models, with implications for haematological fluid dynamics, J. Biomech. 85 (2019) 230–238, http://dx.doi.org/10.1016/j.jbiomech.2019.01.036.

[40] G. Gillispie, P. Prim, J. Copus, J. Fisher, A.G. Mikos, J.J. Yoo, A. Atala, S.J. Lee, Assessment methodologies for extrusion-based bioink printability, Biofabrication 12 (2020) 022003, http://dx.doi.org/10.1088/1758-5090/ab6f0d.

[41] K. Hölzl, S. Lin, L. Tytgat, S.V. Vlierberghe, L. Gu, A. Ovsianikov, Bioink properties before, during and after 3D bioprinting, Biofabrication 8 (2016) 032002, http://dx.doi.org/10.1088/1758-5090/8/3/032002.

[42] J. Groll, J.A. Burdick, D.-W. Cho, B. Derby, M. Gelinsky, S.C. Heilshorn, T. Jüngst, J. Malda, V.A. Mironov, K. Nakayama, A. Ovsianikov, W. Sun, S. Takeuchi, J.J. Yoo, T.B.F. Woodfield, A definition of bioinks and their distinction from biomaterial inks, Biofabrication 11 (2018) 013001, http://dx.doi.org/10.1088/1758-5090/aaec52.

[43] D.M. Binding, An approximate analysis for contraction and converging flows, J. Non-Newton. Fluid Mech. 27 (1988) 173–189, http://dx.doi.org/10.1016/0377-0257(88)85012-2.

[44] B. Debbaut, M. Crochet, Extensional effects in complex flows, J. Non-Newton. Fluid Mech. 30 (1988) 169–184, http://dx.doi.org/10.1016/0377-0257(88)85023-7.

[45] K. Walters, H. Tamaddon-Jahromi, M. Webster, M. Tomé, S. Mckee, The competing roles of extensional viscosity and normal stress differences in complex flows of elastic liquids, Korea Aust. Rheol. J. 21 (2009) 225–233.

[46] M. Hospodiuk, K. Moncal, M. Dey, I. Ozbolat, Extrusion-based biofabrication in tissue engineering and regenerative medicine, in: A. Ovsianikov, J. Yoo, V. Mironov (Eds.), 3D Printing and Biofabrication, Springer International Publishing, Cham, ISBN: 978-3-319-45444-3, 2018, pp. 255–281.

[47] N. Paxton, W. Smolan, T. Böck, F. Melchels, J. Groll, T. Jungst, Proposal to assess printability of bioinks for extrusion-based bioprinting and evaluation of rheological properties governing bioprintability, Biofabrication 9 (2017) 044107, http://dx.doi.org/10.1088/1758-5090/aa8dd8.

[48] G. Cidonio, M. Glinka, J. Dawson, R. Oreffo, The cell in the ink: Improving biofabrication by printing stem cells for skeletal regenerative medicine, Biomaterials 209 (2019) 10–24, http://dx.doi.org/10.1016/j.biomaterials.2019.04.009.

[49] A. Blaeser, D. Duarte Campos, U. Puster, W. Richtering, M. Stevens, H. Fischer, Controlling shear stress in 3D bioprinting is a key factor to balance printing resolution and stem cell integrity, Adv. Healthcare Mater. 5 (2016) 326–333, http://dx.doi.org/10.1002/adhm.201500677.

[50] J. Snyder, A.R. Son, Q. Hamid, C. Wang, Y. Lui, W. Sun, Mesenchymal stem cell printing and process regulated cell properties, Biofabrication 7 (2015) 044106, http://dx.doi.org/10.1088/1758-5090/7/4/044106.

[51] J.-P. Matas, J.F. Morris, E. Guazzelli, Inertial migration of rigid spherical particles in poiseuille flow, J. Fluid Mech. 515 (2004) 171—195, http://dx.doi.org/10.1017/S0022112004000254.

[52] M. Staben, R. Davis, Particle transport in poiseuille flow in narrow channels, Int. J. Multiph. Flow 31 (2005) 529–547, http://dx.doi.org/10.1016/j.ijmultiphaseflow.2004.12.004.

[53] A.A. Bhagat, S. Kuntaegowdanahalli, I. Papautsky, Inertial microfluidics for continuous particle filtration and extraction, Microfluid Nanofluid 7 (2008) 217–226, http://dx.doi.org/10.1007/s10404-008-0377-2.

[54] L. Down, D. Papavassiliou, E. O'Rear, Significance of extensional stresses to red blood cell lysis in a shearing flow, Ann. Biomed. Eng. 39 (2011) 1632–1642, http://dx.doi.org/10.1007/s10439-011-0262-0.

[55] Y. Bae, H. Jang, T.H. Shin, G. Phukan, T. Tran, G. Lee, W.R. Hwang, J. Kim, Microfluidic assessment of mechanical cell damage by extensional stress, Lab Chip 16 (2015) 96–103, http://dx.doi.org/10.1039/c5lc01006c.

[56] J. Korelc, P. Wriggers, Automation of Finite Element Methods, Springer Cham, Switzerland, 2016, http://dx.doi.org/10.1007/978-3-319-39005-5.

[57] P. Wriggers, Nonlinear Finite Element Methods, Springer Berlin Heidelberg, Berlin, Heidelberg, 2008, http://dx.doi.org/10.1007/978-3-540-71001-1.

[58] D. Boffi, F. Brezzi, M. Fortin, Finite elements for the Stokes problem, in: D. Boffi, L. Gastaldi (Eds.), Mixed Finite Elements, Compatibility Conditions, and Applications: Lectures Given At the C.I.M.E. Summer School Held in Cetraro, Italy June 26–July 1, 2006, Springer Berlin Heidelberg, Berlin, Heidelberg, ISBN: 978-3-540-78314-5, 2008, pp. 45–100.

[59] E. Buckingham, On physically similar systems; illustrations of the use of dimensional equations, Phys. Rev. 4 (1914) 345–376, http://dx.doi.org/10.1103/PhysRev.4.345.

[60] Nordson, Optimum disposable reservoir systems, 2023, URL https://www.nordson.com/en/Products/EFD-Products/General-Purpose-Dispense-Tips.

[61] A. Carlier, G.A. Skvortsov, F. Hafezi, E. Ferraris, J. Patterson, B. Koc, H.V. Oosterwyck, Computational model-informed design and bioprinting of cell-patterned constructs for bone tissue engineering, Biofabrication 8 (2016) 025009, http://dx.doi.org/10.1088/1758-5090/8/2/025009.

[62] A. Sedigh, P. Ghelich, J. Quint, E.C. Mollocana-Lara, M. Samandari, A. Tamayol, R.E. Tomlinson, Approximating scaffold printability utilizing computational methods, Biofabrication 15 (2023) 025014, http://dx.doi.org/10.1088/1758-5090/acbbf0.

[63] T. Santner, B. Williams, W. Notz, The design and analysis computer experiments, 2003, http://dx.doi.org/10.1007/978-1-4757-3799-8.

Francesco Chirianni is a Ph.D. student at the University of Rome Tor Vergata in the Department of Civil Engineering and Computer Science Engineering. In 2021 he earned his master's degree cum laude in Mechanical Engineering at the University of Rome Tor Vergata. Francesco Chirianni's research is centered on the computational modeling of extrusion-based technologies, focusing in particular on technologies for tissue engineering.

Giuseppe Vairo is Full Professor in Mechanics of Materials and Structures at the University of Rome Tor Vergata. He was Visiting Professor at the University Pierre et Marie Curie (Sorbonne Universités, 2016). He is author of more than 200 scientific publications (more than 90 peer-reviewed), many lectures in international and national congresses, 2 European Patents. His main research activity focus on: biomechanics of tissues and biological systems; mechanics of advanced materials and smart structures; wind engineering, applied mathematics and numerical methods.

Michele Marino is an Associate Professor at the University of Rome Tor Vergata in the Department of Civil Engineering and Computer Science Engineering. Distinguished as both a Rita Levi Montalcini and an Alexander von Humboldt Fellow, he has also received the AIMETA Junior Prize in Mechanics of Solids and Structures. Michele Marino's research is centered on structural and computational mechanics, particularly in the realm of complex material behaviors. His work extends to addressing multiscale and multiphysics challenges, exploring cardiovascular biomechanics, and advancing enabling technologies for tissue engineering.